Neuron

Article

CLU alleviates Alzheimer's disease-relevant processes by modulating astrocyte reactivity and microglia-dependent synaptic density

Graphical abstract

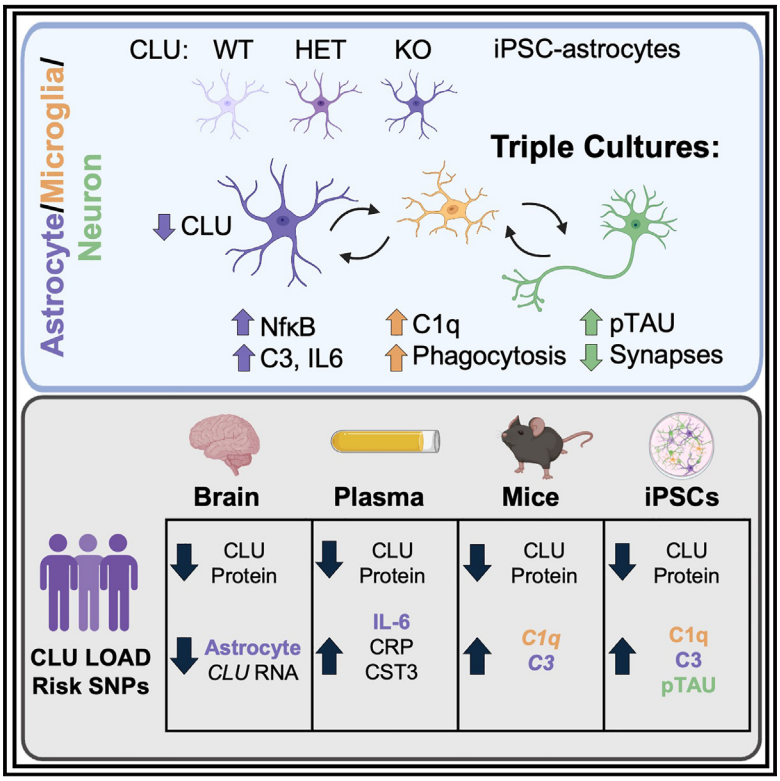

Authors

Alexandra M. Lish, Elyssa F.L. Grogan, Courtney R. Benoit, ..., Philip L. De Jager, Vilas Menon, Tracy L. Young-Pearse

Correspondence

tpearse@bwh.harvard.edu

In brief

Lish et al. reveal that AD-protective *CLU* alleles enhance CLU upregulation in response to accumulated neuropathology, thereby dampening inflammatory signaling between microglia and astrocytes. Using several complementary approaches, they show that CLU upregulation in astrocytes protects neurons from microglia-mediated induction of phospho-tau and synapse loss.

Highlights

- AD-risk SNPs at the *CLU* locus selectively reduce CLU expression in astrocytes
- Increased inflammatory proteins in CLU-deficient and AD *CLU* risk astrocytes
- Microglia mediate CLU-dependent synapse reduction and increased tau phosphorylation
- AD-protective *CLU* alleles disrupt the link between tau pathology and cognition

Lish et al., 2025, Neuron *113*, 1–22
June 18, 2025
https://doi.org/10.1016/j.neuron.2025.03.034

CellPress

Neuron

CellPress

Article

CLU alleviates Alzheimer's disease-relevant processes by modulating astrocyte reactivity and microglia-dependent synaptic density

Alexandra M. Lish,[1] Elyssa F.L. Grogan,[1] Courtney R. Benoit,[1] Richard V. Pearse II,[1] Sarah E. Heuer,[1] Tain Luquez,[4] Gwendolyn A. Orme,[1] Paige C. Galle,[1] Giedre Milinkeviciute,[5] Kim N. Green,[5,6] Kellianne D. Alexander,[1] Seeley B. Fancher,[1] Andrew M. Stern,[1] Masashi Fujita,[4] David A. Bennett,[3] Nicholas T. Seyfried,[2] Philip L. De Jager,[4] Vilas Menon,[4] and Tracy L. Young-Pearse[1,7,*]

[1]Ann Romney Center for Neurologic Diseases, Department of Neurology, Brigham and Women's Hospital and Harvard Medical School, Boston, MA, USA

[2]Department of Biochemistry, Emory School of Medicine, Atlanta, GA, USA

[3]Rush Alzheimer's Disease Center, Rush University Medical Center, Chicago, IL, USA

[4]Center for Translational and Computational Neuroimmunology, Department of Neurology and the Taub Institute for the Study of Alzheimer's Disease and the Aging Brain, Columbia University Irving Medical Center, New York, NY, USA

[5]Institute for Memory Impairment and Neurological Disorders, University of California, Irvine, Irvine, CA, USA

[6]Department of Neurobiology and Behavior, School of Biological Sciences, University of California, Irvine, Irvine, CA, USA

[7]Lead contact

*Correspondence: tpearse@bwh.harvard.edu

https://doi.org/10.1016/j.neuron.2025.03.034

SUMMARY

Genetic studies implicate clusterin (CLU) in the pathogenesis of Alzheimer's disease (AD), yet its precise molecular impact remains unclear. Through unbiased proteomic profiling and functional validation in CLU-deficient astrocytes, we identify increased nuclear factor κB (NF-κB)-dependent signaling and complement C3 secretion. Reduction of astrocyte CLU induced microglia-dependent modulation of extracellular apolipoprotein E (APOE) and phosphorylated tau, as well as increased microglial phagocytosis and reduced synapse numbers. By integrating mouse and human cellular models with comprehensive analyses of human plasma and brain tissue, we demonstrate that *CLU* AD-risk alleles are associated with reduced CLU protein and heightened inflammatory profiles. These findings establish a mechanistic link between AD genetic risk factors, astrocyte reactivity, and microglia-mediated effects on synaptic integrity. Collectively, these results support a model in which CLU upregulation in response to neuropathology is associated with maintenance of cognitive function, while diminished astrocyte CLU levels heighten disease susceptibility.

INTRODUCTION

Elevated clusterin (CLU) levels are consistently observed in the brain tissue and cerebrospinal fluid of individuals with Alzheimer's disease (AD),[1–6] a disease characterized by the accumulation of amyloid beta (Aβ) plaques and neurofibrillary tau tangles. Despite this, the role of CLU in AD remains unclear, with conflicting evidence as to whether it is neuroprotective, pathogenic, or simply a byproduct of disease. Genome-wide association studies (GWASs) have identified intronic single-nucleotide polymorphisms (SNPs) at the *CLU* locus that significantly influence late-onset AD (LOAD) risk.[7,8] However, the effects of these SNPs on CLU expression are inconsistent, with studies reporting both decreases[9–12] and increases[13–16] in expression levels. While CLU is expressed across various brain cell types, the cell-specific effects of these LOAD-associated SNPs and their broader impact on cellular function remain poorly understood.

CLU is a secreted molecular chaperone that binds misfolded proteins, facilitating their clearance through receptor-mediated endocytosis. In AD, CLU localizes to Aβ plaques,[17–19] modulates Aβ aggregation, and promotes clearance,[20–23] supporting a neuroprotective role. It also accumulates at synapses, with astrocyte-secreted CLU shown to regulate excitatory synaptic transmission and spine density in mouse models.[24,25] Beyond these roles, CLU participates in lipid metabolism,[26] complement inhibition,[27] apoptosis,[28] and inhibition of nuclear factor-κB (NF-κB) activity.[29–32] While these studies have advanced our understanding of CLU biology, they have largely relied on mouse models or investigated CLU's role outside the brain. To determine whether and how CLU may interact with these cellular processes to affect AD risk, it is crucial to employ a physiologically relevant system in which CLU is expressed at endogenous levels in human brain cells.

Please cite this article in press as: Lish et al., CLU alleviates Alzheimer's disease-relevant processes by modulating astrocyte reactivity and microglia-dependent synaptic density, Neuron (2025), https://doi.org/10.1016/j.neuron.2025.03.034

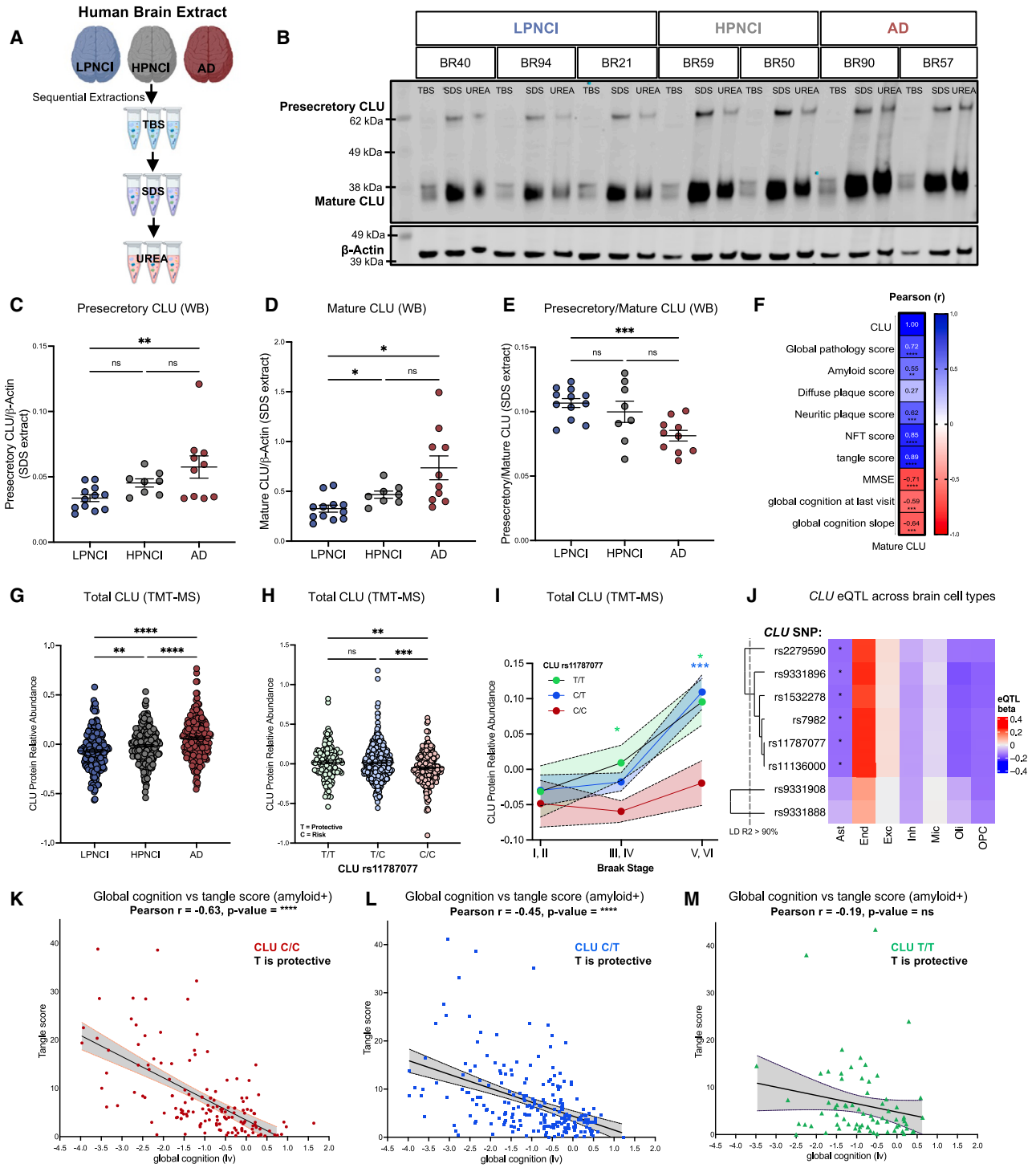

Figure 1. *CLU* risk alleles are associated with reduced CLU expression in astrocytes in the human brain

(A) *Postmortem* human brain extracts from LPNCI ($N = 12$), HPNCI ($N = 8$), and AD ($N = 10$) groups were sequentially extracted using TBS, SDS, and urea. LPNCI, low neuropathology, not cognitively impaired; HPNCI, high neuropathology, not cognitively impaired; AD, pathological and clinical Alzheimer's diagnosis. See Table S1.

(B) Representative western blot (WB) of CLU and β-actin (full dataset in Figure S1A).

(C–E) Quantification of presecretory CLU (C), mature CLU (D), and their ratio (E) normalized to β-actin. See Figures S1B–C for additional quantifications.

(F) Pearson correlations of mature CLU (urea fraction) with neuropathological and cognitive scores.

(legend continued on next page)

Please cite this article in press as: Lish et al., CLU alleviates Alzheimer's disease-relevant processes by modulating astrocyte reactivity and microglia-dependent synaptic density, Neuron (2025), https://doi.org/10.1016/j.neuron.2025.03.034

The need for human *in vitro* models is especially critical for capturing and dissecting the mechanisms of intercellular signaling, given the intricate interplay between innate immune activation, complement signaling, and synapse loss in AD. Amyloid plaques trigger microglial activation,[33–35] leading to the release of proinflammatory molecules such as tumor necrosis factor (TNF), interleukin-1a (IL1α), and complement component 1q (C1q).[36] These molecules drive neurotoxic astrocyte reactivity characterized by NF-κB activation and increased complement C3 secretion. Combined, these proinflammatory states disrupt brain homeostasis and promote neurodegeneration. The complement system plays a central role in this process, regulating synapse pruning and microglial phagocytosis through the involvement of complement proteins such as C3 and C1q.[37–39] In disease, the complement system becomes excessively activated in response to neuronal damage, including exposure to Aβ,[40–42] which may contribute to synapse loss and neurodegeneration (reviewed in Batista et al.[43]). Although CLU has been suggested to modulate the complement cascade, NF-κB signaling, and synaptic transmission in non-human models, it remains unclear whether and how CLU might mediate crosstalk between these signaling cascades to influence human disease risk.

Here, we conducted in-depth, multi-omic *postmortem* studies of human brain tissue from several hundred individuals and found that CLU expression is higher in AD brain tissue. Importantly, however, CLU protein and RNA levels, specifically in astrocytes, were lower in individuals carrying *CLU* risk alleles. Proteomic and functional studies revealed that CLU reduction (heterozygous, HET) or loss (knockout, KO) in human induced pluripotent stem cells (hiPSC)-derived astrocytes drives heightened reactivity, including increased secretion of C3 and inflammatory proteins, which were rescued by CLU overexpression or NF-κB inhibition. Using co-cultures comprising astrocytes, neurons, and microglia, we demonstrate an essential requirement for microglia in mediating CLU-dependent modulation of apolipoprotein E (APOE) and phosphorylated tau levels. CLU-deficient astrocytes also induced a reduction in synapse numbers and increased microglial phagocytosis. Across experimental models, we observed parallels between CLU deficiency and the effects of *CLU* LOAD risk SNPs. *In vivo*, mice carrying a humanized *CLU* risk allele showed reduced CLU protein levels and increased expression of phagocytosis- and complement-related genes. Longitudinal plasma analyses revealed that individuals with protective *CLU* alleles exhibited increased CLU levels without changes in inflammatory markers, whereas those with risk alleles did not exhibit an increase in CLU levels but showed elevated inflammatory markers over time. Finally, genetically diverse iPSC-derived astrocytes (iAs) demonstrated that *CLU* risk alleles were associated with reduced CLU and APOE levels and increased complement protein and phosphorylated tau levels when co-cultured with familial AD (fAD) neurons and *APOE4* microglia. These data culminate in support of a new paradigm regarding CLU biology: efficient CLU upregulation in response to Aβ and tau accumulation can prevent dysregulated inflammatory signaling between astrocytes and microglia, thereby protecting against neurodegeneration and cognitive decline.

RESULTS

AD *CLU* risk alleles are associated with reduced CLU expression in astrocytes in the human brain

To conclusively determine the levels of CLU in individuals with AD and the association of risk SNPs at the *CLU* locus with CLU levels,[1–4,44] we analyzed human brain tissue from hundreds of deeply phenotyped participants in the Religious Orders Study and Rush Memory and Aging Projects (ROSMAP).[45–48] Protein expression of CLU was assessed using western blot (WB) and tandem mass tag-mass spectrometry (TMT-MS). We compared CLU levels across three categories of individuals: low neuropathology, not cognitively impaired (LPNCI), high neuropathology, not cognitively impaired (HPNCI), and AD. LPNCI individuals had neither a clinical nor neuropathological diagnosis of AD, HPNCI had a neuropathological diagnosis of AD with no cognitive impairment, and AD individuals had both a neuropathological and clinical diagnosis.[45,49]

Brain tissue from 30 individuals was homogenized using sequential extraction in tris-buffered saline (TBS), sodium dodecyl sulfate (SDS), and urea (Figure 1A; Table S1). WB analysis with an antibody recognizing the α-chain of CLU detected two bands: a 68 kDa immature presecretory form and a 37 kDa mature processed form (Figures 1B and S1A). CLU expression was elevated in AD individuals across all extractions and both forms of CLU (Figures 1C, 1D, and S1C), but the presecretory-to-mature CLU ratio was lower in AD (Figure 1E), suggesting increased processing through the secretory pathway. As expected, CLU protein levels correlated strongly with neuropathological measurements from the same individuals (Figure 1F). However, it is notable that the correlation between CLU and tangle score is much stronger than with the β-amyloid score. TMT-MS analysis of urea-extracted CLU protein from 702 ROSMAP brains[50] confirmed higher CLU expression in HPNCI and AD individuals compared with LPNCI (Figure 1G), with females trending toward higher expression in AD (Figure S2J). However, individuals homozygous for the risk C allele of rs11787077 exhibited lower CLU levels (Figure 1H),

(G and H) CLU levels in ROSMAP brain samples (urea extracts, TMT-MS) by diagnosis (G; $N = 236$ LPNCI, 230 HPNCI, and 236 AD) and rs11787077 genotype (H; $N = 134$ T/T, 245 C/C, and 390 C/T). See Figure S2H for (G) stratified by CLU peptide.
(I) CLU levels from (H), further stratified by Braak stage and genotype, with significant reductions in C/C vs. T/T or C/T at stages 3–4 and 5–6 (two-way ANOVA with Dunnett's multiple comparisons test). See Figures S2L–S2N.
(J) Heatmap of *CLU* eQTL summary statistics for eight SNPs across brain cell types. *FDR < 0.05. See Table S2.
(K–M) Pearson correlations between *postmortem* tangle score and global cognition in amyloid-positive (see STAR Methods) ROSMAP participants, stratified by rs11787077 genotype ($N = 147$ C/C, 222 C/T, and 72 T/T). Shaded area indicates 95% confidence interval.
For all graphs, data are mean ± SEM. One-way ANOVA with Tukey's multiple comparisons test: ****$p < 0.0001$, ***$p < 0.001$, **$p < 0.01$, *$p < 0.05$; ns, not significant.
See also Table S1.

Please cite this article in press as: Lish et al., CLU alleviates Alzheimer's disease-relevant processes by modulating astrocyte reactivity and microglia-dependent synaptic density, Neuron (2025), https://doi.org/10.1016/j.neuron.2025.03.034

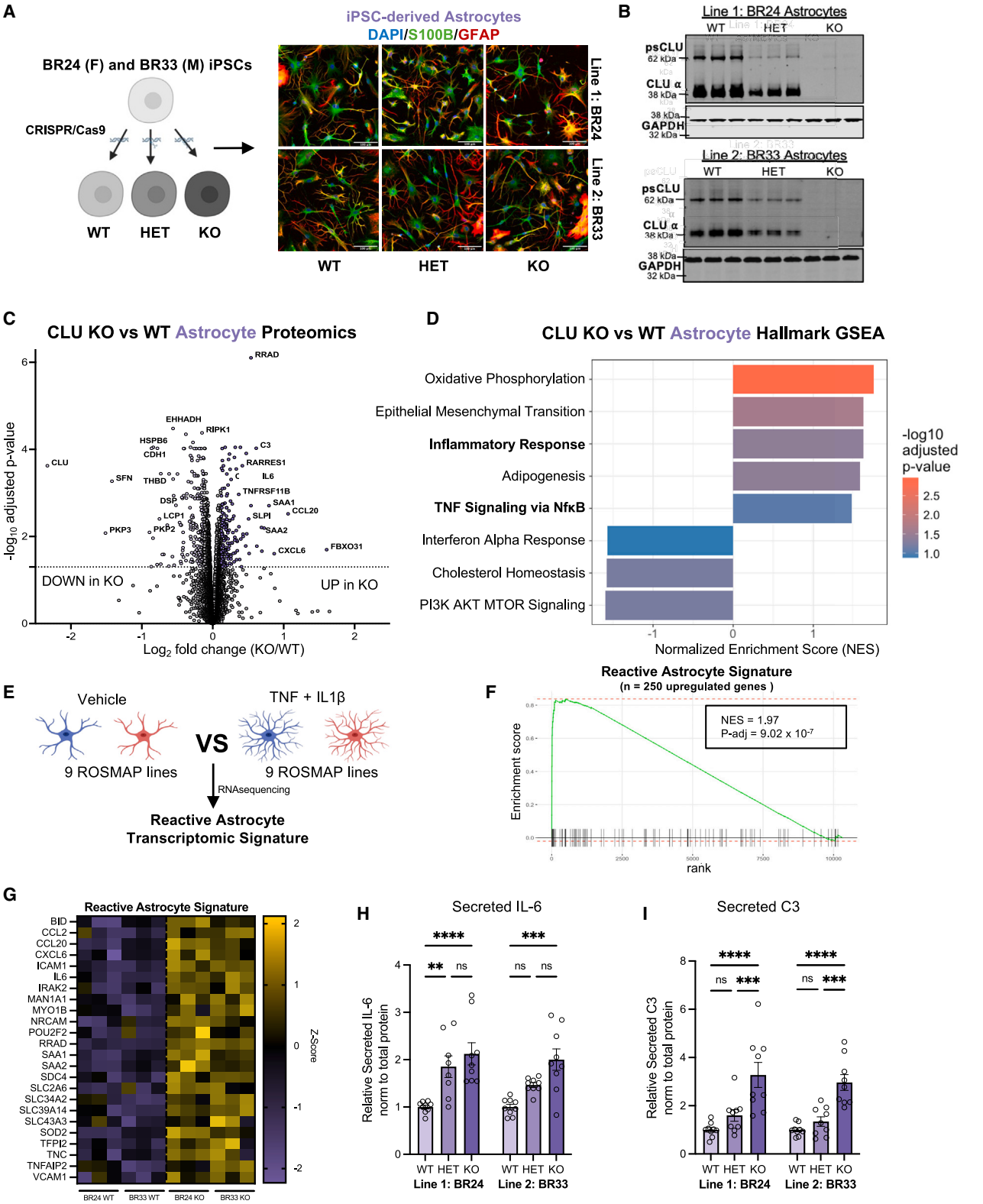

Figure 2. CLU deficiency amplifies astrocyte reactivity and inflammatory signatures

(A) Representative immunostaining of CLU WT, HET, and KO astrocytes derived from two iPSC lines (BR33 and BR24), labeled for GFAP (red) and S100B (green). Scale bar, 100 μM. See Figures S3A and S3B for clone details.

(legend continued on next page)

Please cite this article in press as: Lish et al., CLU alleviates Alzheimer's disease-relevant processes by modulating astrocyte reactivity and microglia-dependent synaptic density, Neuron (2025), https://doi.org/10.1016/j.neuron.2025.03.034

a trend observed across 12 of 16 CLU peptides spanning both α- and β-chains (Figures S1D–E). Since CLU expression correlated strongly with tangle score, we further analyzed its levels across Braak stages. Strikingly, CLU levels were significantly elevated in later Braak stages only in individuals carrying the protective "T" allele (Figures 1I and S2L–S2N).

Although *CLU* is broadly expressed across cell types, the contribution of each to *CLU* expression patterns in relation to risk alleles remains unclear. Using pseudobulk analysis of single-nucleus RNA sequencing (snRNA-seq) from over 400 ROSMAP participants,[51] we found that *CLU* is widely expressed but highest in astrocytes (Figures S2A and S2B). Human cellular models confirmed that astrocytes secrete the highest levels of CLU compared with neurons and microglia (Figure S2C). Several AD-associated *CLU* risk SNPs identified by GWAS were linked to lower *CLU* expression specifically in astrocytes, with no significant changes in neurons or microglia (Figures 1J and S2D–S2G; Table S2). Notably, in individuals with a high neuropathological burden, the strongest association was observed between lower CLU expression and the rs11787077-C risk allele (Figures S2H–I).

To evaluate the impact of *CLU* risk alleles on cognitive function in the aged brain, we compared individuals carrying risk versus protective alleles. The ROS and MAP cohorts provide detailed *postmortem* neuropathological reports,[47] enabling comprehensive genetic association analyses. Among individuals with amyloid pathology (as assessed by immunostaining, β-amyloid score > 1),[52–54] those with the *CLU* rs11787077-C risk allele had worse global cognition (Figure S2K). Additionally, tangle score was negatively correlated with cognition in individuals with *CLU* risk alleles (Figures 1K and 1L), whereas this association was absent in those with the protective variant (Figure 1M). Taken together, these findings support the hypothesis that CLU is upregulated as a protective response to accumulating neuropathology. However, lower levels of CLU, specifically in astrocytes, are associated with an increased risk of cognitive decline and AD. This dual pattern of CLU regulation highlights its pivotal role in the pathophysiology of AD and underscores the critical need to further investigate the molecular consequences of reduction of CLU in human astrocytes.

CLU deficiency induces protein-level changes consistent with elevated astrocyte reactivity

To investigate CLU's role in human cells, we used CRISPR-Cas9 to generate isogenic CLU wild-type (WT), HET, and KO iPSC lines in two genetic backgrounds (Figures S3A and S3B). These iPSCs were differentiated into astrocytes,[55,56] confirmed by glial fibrillary acidic protein (GFAP) and S100 calcium binding protein B (S100B) expression and acquisition of a characteristic star-like morphology (Figure 2A). WB and ELISA analyses showed ∼50% CLU reduction in HET lines and complete loss in KO lines (Figure 2B). To assess protein-level disruptions from CLU loss, we performed TMT-MS on WT and KO iAs. Among 396 differentially expressed proteins (DEPs) consistently altered across both genetic backgrounds (Figure 2C; Table S3), CLU KO astrocytes exhibited upregulation of proinflammatory cytokines (interleukin-6, IL-6), chemokines (CXCL6 and CCL20), and complement components (C3). Gene set enrichment analysis (GSEA) against the Hallmark gene set[57] revealed increased inflammatory responses and reduced cholesterol homeostasis in CLU KO astrocytes (Figure 2D; Table S3).

To further investigate the inflammatory response, we analyzed a transcriptomic dataset from iAs recently described by our group.[56] In this dataset, nine iA lines from ROSMAP donors were treated with vehicle or TNF + IL-1β and profiled by bulk RNA-seq (Figure 2E). We generated a custom human reactive astrocyte signature by ranking the top upregulated differentially expressed genes (DEGs) ($-\log_{10}$ adjusted p value × $\log_2$ fold change) in response to TNF + IL-1β. Applying this signature to our CLU astrocyte proteomics dataset revealed significant enrichment of reactive astrocyte proteins in CLU KO astrocytes (Figure 2F). Leading-edge proteins included direct NF-κB targets such as IL-6, CCL2, and intercellular adhesion molecule 1 (ICAM-1) (Figure 2G). Example gene bar plots highlight CCL20, a top transcript upregulated by TNF + IL-1β, and ras-related glycolysis inhibitor and calcium channel regulator (RRAD), the strongest DEP in CLU KO astrocytes (Figures S3C and S3D). To confirm that CLU loss mimics the proteomic profile of cytokine-stimulated astrocytes, we analyzed secreted proteins in iA cultures. Consistent with our proteomics data, CLU loss led to increased secretion of IL-6, C3, serum amyloid A (SAA), and ICAM-1 (Figures 2H, 2I, and S4A–S4D). WB further confirmed elevated intracellular ICAM-1 in CLU-deficient astrocytes (Figures S4E–F). Notably, CLU overexpression rescued the elevated C3 and IL-6 levels observed with CLU KO (Figures 3A–3D). These findings indicate that CLU deficiency amplifies astrocyte inflammatory responses.

Heightened levels of C3 and inflammatory response genes in CLU-deficient astrocytes are NF-κB dependent

Previous studies in mouse models and immortalized cell lines suggest that CLU regulates NF-κB signaling.[29–32] Here, we examined whether CLU loss affects canonical NF-κB signaling in human astrocytes by quantifying IκBα protein levels and NF-κB reporter activity. NF-κB activation is marked by decreased IκBα levels, which becomes degraded upon activation.[58] WB

(B) Representative WB of CLU WT, HET, and KO iAs, probed for CLU and GAPDH.
(C) Volcano plot of differential protein expression (KO vs. WT, TMT-MS). Purple, adjusted $p < 0.01$, $\log_2FC > 0.12$ or < -0.12. See Table S3.
(D) GSEA of hallmark pathways from differential protein expression analysis. See Table S3.
(E) Schematic of RNA-seq experimental design (nine ROSMAP iA lines, vehicle, or TNF + IL-1β; dataset from Lee et al.[56]).
(F) GSEA of TNF + IL-1β-activated targets (top 250, ranked by $-\log_{10}$ adjusted p value × $\log_2FC$) in CLU KO vs. WT iAs.
(G) Heatmap of leading-edge genes upregulated with TNF + IL-1β and in CLU KO vs. WT iAs.
(H and I) Secreted IL-6 and C3 levels in CLU WT, HET, and KO astrocytes (ELISA, normalized to total protein and WT). Data shown as mean ± SEM.
(B–H) $N = 2$ genetic backgrounds, 6 differentiations, and 3 wells per differentiation. Two-way ANOVA with Sidak's multiple comparisons test, $^{****}p < 0.0001$, $^{***}p < 0.001$, $^{**}p < 0.01$; ns, not significant.
See also Table S3.

Please cite this article in press as: Lish et al., CLU alleviates Alzheimer's disease-relevant processes by modulating astrocyte reactivity and microglia-dependent synaptic density, Neuron (2025), https://doi.org/10.1016/j.neuron.2025.03.034

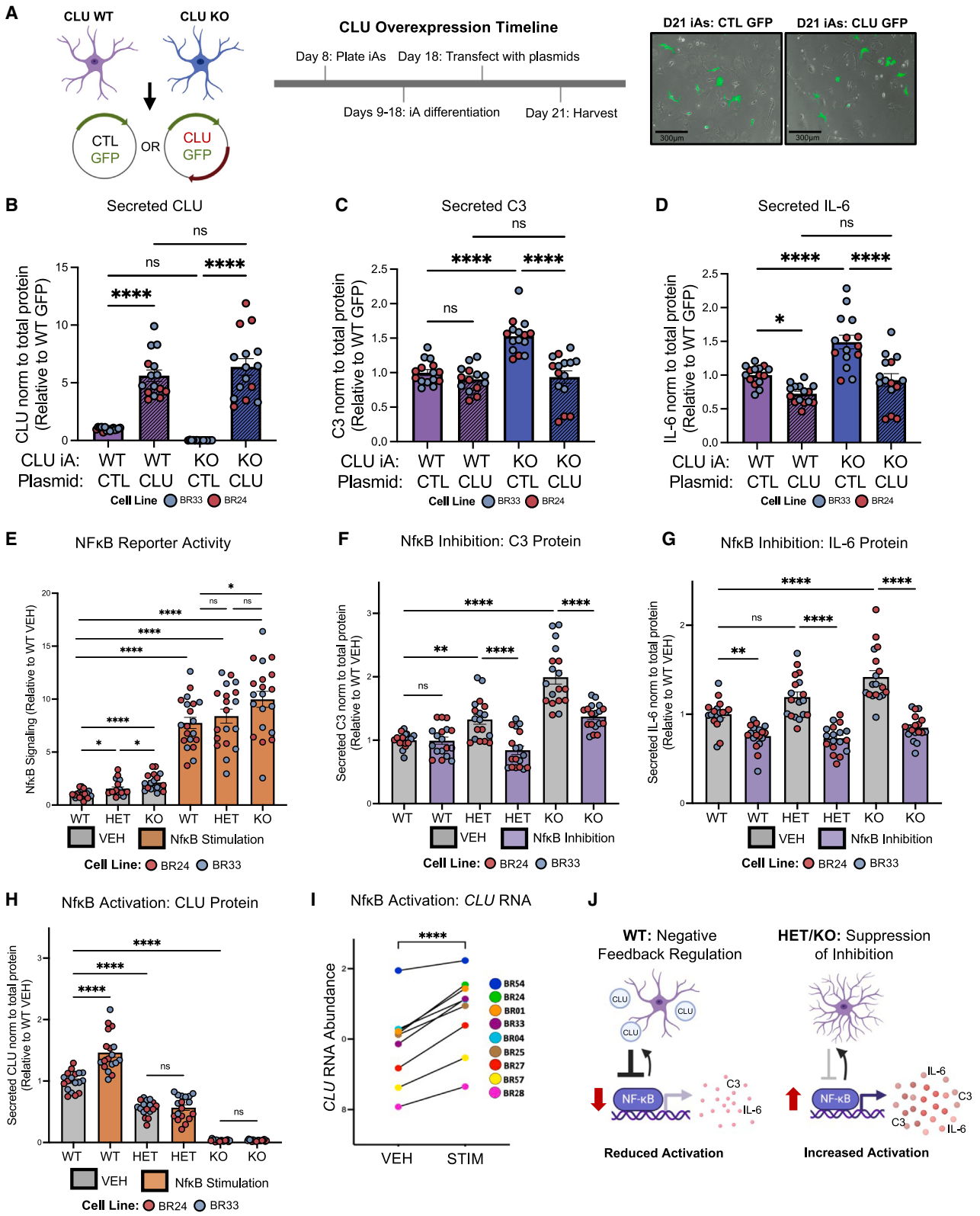

Figure 3. Heightened levels of C3 and inflammatory response genes in CLU-deficient astrocytes are NF-κB dependent

(A) Schematic and timeline for CLU overexpression and control (CTL) transfections. Representative GFP and brightfield images of transfected iAs. Scale bar, 300 μm.

(legend continued on next page)

analysis of CLU WT, HET, and KO iAs showed a reduction in IκBα levels after TNF + IL-1β stimulation and a baseline decrease in CLU HET and KO iAs (Figures S4G and S4H). A luciferase-based NF-κB reporter assay[59] revealed elevated baseline NF-κB signaling in CLU HET and KO iAs (Figures 3E and S4I), with increased luciferase activity upon cytokine stimulation in all cultures. These results suggest CLU deficiency enhances baseline NF-κB signaling in human astrocytes.

Complement protein C3 has been previously defined as an astroglial target of NF-κB.[60,61] To determine whether upregulations of C3 and other inflammatory markers in CLU-deficient iAs are NF-κB dependent, we treated cultures with an NF-κB inhibitor. Baseline RNA and protein levels of C3 were elevated in CLU HET and KO vehicle-treated cultures (Figures 3F and S4J), but NF-κB inhibition significantly reduced C3 levels in these cells, with no effect in WT iAs. Similarly, elevated IL-6 and CCL2 expression in CLU HET and KO iAs was attenuated by NF-κB inhibition (Figures 3G, S4K, and S4L). These findings demonstrate that the heightened inflammatory response in CLU-deficient astrocytes is driven by increased NF-κB signaling. To assess whether NF-κB activation regulates CLU expression, we measured CLU RNA and protein levels in iA cultures following NF-κB stimulation (Figures 3H and S4M). WT iAs responded by upregulating CLU transcription and secretion, a finding confirmed in an independent set of nine ROSMAP iA lines (Figure 3I). These results suggest that CLU provides negative feedback to regulate NF-κB signaling in human astrocytes (Figure 3J). In the following sections, we investigate the impact of CLU deficiency and the resulting inflammatory environment on neuron and microglia biology.

Microglia are essential in mediating CLU-dependent reduction of APOE and elevated phosphorylated tau levels in co-cultures of neurons, astrocytes, and microglia

To investigate the non-autonomous effects of astrocytic CLU on neurons and microglia, we used transwell-based co-cultures (Figures S5A–S5D). After 3 days, iPSC-derived neurons (iNs) and iPSC-derived microglia (iMGs) co-cultured with CLU WT vs. KO iAs were harvested for TMT-MS, showing minimal differences (Figures S5A–S5L; Table S4). These subtle effects suggest that longer co-culture durations and direct contact may be needed for the full spectrum of signaling between these cell types. Thus, we extended the co-culture to 6 days using a tri-culture system of iNs, iAs, and iMGs (Figures S5M and S5N). Immunostaining and WB confirmed the presence of TUJ1+ neurons, IBA1+ microglia, and CD44+ astrocytes (Figures 4A, 4B, and S5O). As expected, CLU protein levels were reduced in CLU KO astrocyte tri-cultures (Figure 4C), which also exhibited decreased APOE secretion (Figure 4D), consistent with astrocyte-microglia co-culture findings (Figure S5H). Although CLU and APOE are expressed across multiple cell types, astrocytes are the primary source of their secretion (Figures S5P and S5Q).

CLU plays a well-established role in Aβ clearance through receptor-mediated endocytosis and inhibition of Aβ oligomerization and aggregation.[62–66] However, investigations into CLU's interaction with tau pathology remain limited.[67,68] Our human brain analyses revealed a strong association between CLU and tau accumulation, prompting us to investigate whether astrocytic CLU loss affects tau biology in human cells. Tri-cultures with CLU KO astrocytes exhibited elevated phosphorylated tau relative to total tau (Figures 4E–4H, S6A, and S6B). If CLU directly influences neuronal tau pathology, then it is plausible that microglia are not necessary in these cultures to induce this neuronal phenotype. To ascertain this, we established neuron-astrocyte co-cultures under the same conditions but without microglia (Figures 4I and 4J). Notably, CLU KO astrocytes had no significant impact on phosphorylated tau or APOE levels in these cultures (Figures 4K, 4L, and S6C). These findings suggest that microglia are essential for CLU-dependent regulation of APOE levels and tau phosphorylation.

CLU deficiency in astrocytes leads to reduced synapse number in neurons and increased phagocytosis in microglia

To investigate microglial contributions to CLU-mediated neuronal phenotypes, we performed single-cell RNA sequencing (scRNA-seq) on microglia and neurons co-cultured with CLU WT or KO astrocytes. Importantly, scRNA-seq served as a hypothesis-generating tool, with key findings validated through complementary experimental approaches across multiple differentiations. Uniform manifold approximation and projection (UMAP) clustering identified three major cell types—neurons, astrocytes, and microglia—across seven subclusters (Figures S7A and S7B). Despite astrocytes making up ∼15% of the culture (Figure S5N), their recovery for scRNA-seq was poor, a known challenge in the field.[69,70] No significant shifts in neuron or microglia cluster membership were observed between CLU WT and KO conditions (Figures 4M and S7A–S7H). We first analyzed DEGs in microglia co-cultured with CLU KO vs. WT astrocytes (Figure 4N; Table S5). Notable DEGs included genes related to the complement system (*C1QA*, *C1QB*, and *C1QC*), phagocytosis (*FCGR1A* and *SYK*), and AD-risk genes (*APOE*, *INPP5D*, and

(B–D) ELISA measurements of CLU, C3, and IL-6 in CLU WT, HET, and KO iAs, normalized to total protein and WT CTL.
(E) NF-κB luciferase reporter activity in CLU WT, HET, and KO iAs treated with vehicle or TNF + IL-1β (normalized to Renilla luciferase expression). See Figure S4I for constructs and timeline.
(F and G) ELISA measurements of secreted IL-6 and C3 following 24 h treatment with vehicle or IκB kinase (IKK) Inhibitor VII, normalized to total protein and WT vehicle.
(H) Secreted (ELISA) CLU protein levels following 24 h TNF + IL-1β treatment, normalized to total protein and WT vehicle.
(I) RNA-seq analysis of CLU expression in ROSMAP iAs treated with vehicle or TNF + IL-1β; paired Student's t test (two-tailed), $^{****}p < 0.0001$. Data from Lee et al.[56]
(J) Speculative model of CLU-mediated NF-κB regulation in astrocytes. CLU loss suppresses NF-κB inhibition, increasing C3 and IL-6 secretion.
Data shown as mean ± SEM.
(B–H) $N = 2$ genetic backgrounds, 4–6 differentiations, and 3 wells per differentiation. One-way ANOVA with Sidak's multiple comparisons test, $^{****}p < 0.0001$, $^{***}p < 0.001$, $^{**}p < 0.01$, $^{*}p < 0.05$; ns, not significant.

Please cite this article in press as: Lish et al., CLU alleviates Alzheimer's disease-relevant processes by modulating astrocyte reactivity and microglia-dependent synaptic density, Neuron (2025), https://doi.org/10.1016/j.neuron.2025.03.034

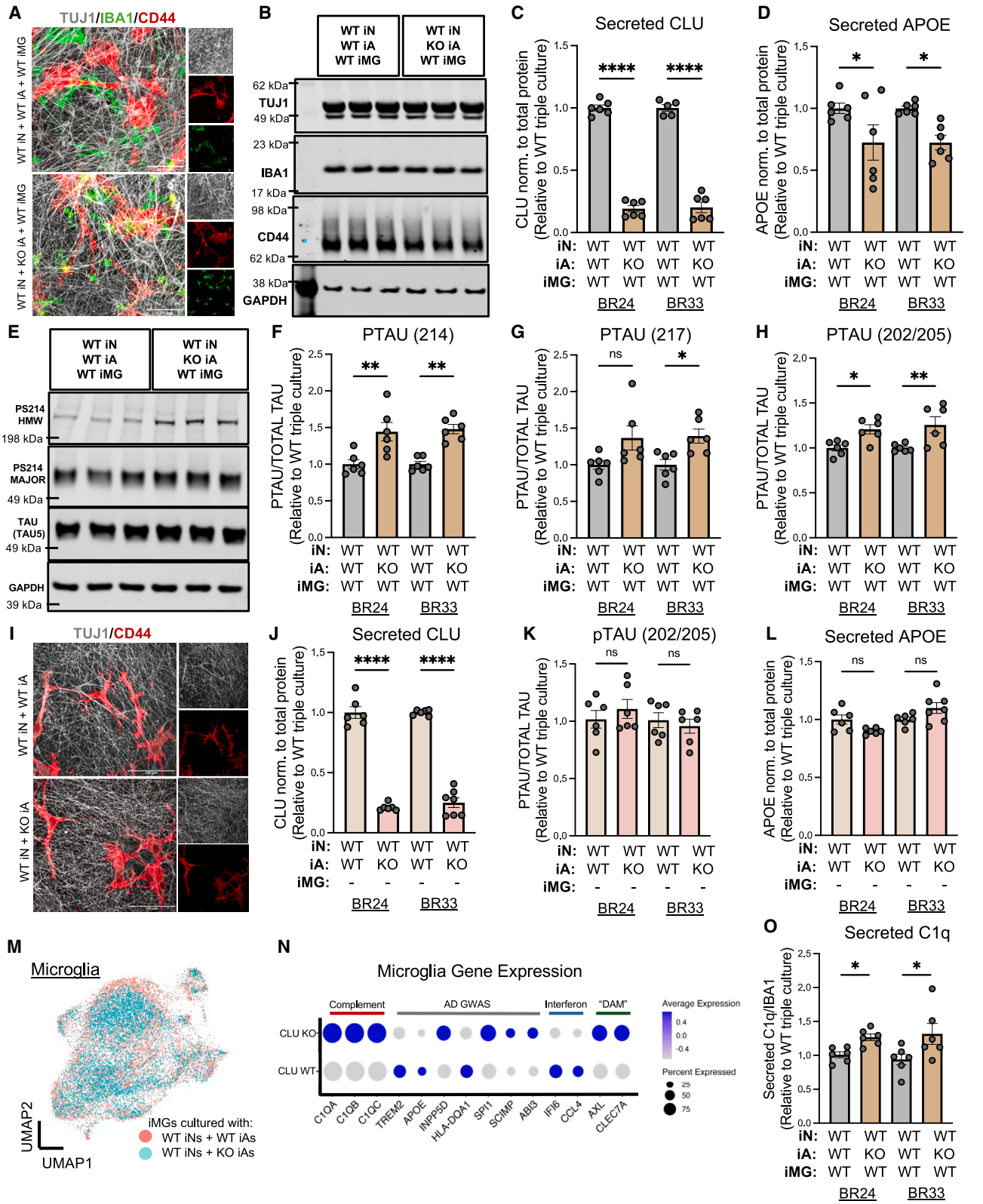

(legend on next page)

Please cite this article in press as: Lish et al., CLU alleviates Alzheimer's disease-relevant processes by modulating astrocyte reactivity and microglia-dependent synaptic density, Neuron (2025), https://doi.org/10.1016/j.neuron.2025.03.034

TREM2). Several disease-associated microglia (DAM) markers (*AXL* and *CLEC7A*)[71] were also differentially expressed. The reduction in *APOE* aligns with our previous transwell and tri-culture findings, which showed decreased APOE protein levels in CLU-deficient conditions (Figures 4D, S5G, and S5H). Additionally, transwell proteomics revealed elevated C1q proteins in microglia co-cultured with CLU KO astrocytes (Figures S5J–S5L; Table S4), a finding validated at the protein level in tri-culture (Figure 4O). We also observed a downward trend in reduction of triggering receptor expressed on myeloid cells 2 (*TREM2*) RNA levels in microglia co-cultured with CLU KO iAs (adjusted p value = 0.11, Table S5). Given TREM2's reported role as a CLU receptor[72] and its involvement in tau and complement activity,[73–75] we measured TREM2 protein levels, which were reduced in CLU KO tri-cultures (Figures S6E and S6F), though the effect size was modest and varied across cell lines.

Microglia-secreted C1q, TNF, and IL-1α are known to induce astrocyte reactivity.[36] Previously, we showed that microglia-astrocyte co-culture increases TREM2 protein expression (A.M.L. et al., unpublished data), while the reactive astrocyte cocktail (C1q, TNF, IL-1α) reduces TREM2 protein.[76] Given that CLU KO astrocytes exhibit elevated C3 and other reactive astrocyte markers, and that microglia exposed to CLU KO astrocytes secrete more C1q, we hypothesized that C1q treatment alone could phenocopy some aspects of CLU KO. To test this, we treated WT neuron-microglia-astrocyte tri-cultures, neuron-astrocyte co-cultures, and microglia monocultures with either vehicle or C1q (Figure 5A). In tri-cultures, C1q treatment significantly reduced TREM2 and APOE levels while increasing phosphorylated tau (Figures 5B, 5C, and S6D–S6I). These effects were absent in neuron-astrocyte co-cultures and microglia monocultures, suggesting that C1q phenocopies CLU deficiency but still requires microglia-astrocyte interaction to influence phosphorylated tau levels (Figure S6J).

To assess how astrocytic CLU loss affects neurons beyond tau changes, we analyzed scRNA-seq data from neurons co-cultured with CLU KO vs. WT astrocytes (Table S5 and Figure S7). GSEA revealed significant dysregulation of synaptic function pathways in CLU KO co-cultures (Figure S7I; Table S5). Given this and the upregulation of complement proteins C3 and C1q in CLU-deficient conditions, we investigated whether CLU loss alters synaptic dynamics. Using 1,1′-dioctadecyl-3,3,3′,3′-tetramethylindocarbocyanine perchlorate (DiI) membrane labeling, we found that neurons in CLU KO astrocyte tri-cultures exhibited reduced spine density but no changes in spine morphology (Figures 5D–5F). To further assess synaptic density, we co-stained neurons for the presynaptic marker VGLUT2 and the postsynaptic marker HOMER1, quantifying colocalized puncta on TUJ1-labeled neurites (Figures 5G and S7J). Automated CellProfiler analysis confirmed a decrease in synapse density in CLU KO tri-cultures (Figures 5H and 5I). Notably, this effect was microglia-dependent, highlighting the role of CLU in maintaining synaptic integrity through neuron-astrocyte-microglia interactions.

Given the microglia-dependent synapse loss in CLU-deficient cultures (Figures 5H and 5I), we examined microglial phagocytosis. Microglia-astrocyte co-cultures were treated with pHrodo-labeled synaptosomes, a pH-sensitive dye that fluoresces upon acidification in phagolysosomes.[77,78] As a negative control, cytochalasin D, an actin polymerization inhibitor, was included (Figure 5J). Both live imaging (Incucyte) and flow cytometry of CD11b+ P2RY12+ microglia showed increased synaptosome uptake in HET and KO astrocyte co-cultures compared with WT (Figures 5K, 5L, and S7K). Additionally, C1q secretion was elevated in CLU HET and KO co-cultures (Figure 5M). Taken together, our findings demonstrate that CLU depletion in astrocytes creates a reactive astrocyte-like environment, marked by enhanced NF-κB signaling and increased C3 secretion. This coincides with intercellular interactions between astrocytes and microglia, resulting in increased microglial phagocytosis and reduced synaptic density (Figure 5N).

CLU risk alleles are associated with reduced CLU expression and increased inflammatory profiles across experimental models

Having shown that CLU deficiency disrupts microglia-astrocyte communication, we next examined whether similar dysfunction occurs with *CLU* risk and protective alleles. To address this, we first utilized an *in vivo* mouse model in which CRISPR was used to substitute a 2 kb region of human CLU containing the enhancer region and the GWAS AD-risk *rs2279590* SNP variant for the orthologous region of CLU within the C57BL/6J mouse genome (generously shared by the Model Organism Development and Evaluation for Late-onset Alzheimer's Disease consortium [MODEL-AD] center at University of California, Irvine

Figure 4. Microglia are essential in mediating CLU-dependent loss of APOE and elevated phosphorylated tau levels in co-cultures of neurons, astrocytes, and microglia

(A) Representative immunostaining of tri-cultures: TUJ1 (neurons, gray), IBA1 (microglia, green), and CD44 (astrocytes, red). Scale bar, 100 μM.
(B) WB of cell-type markers (TUJ1, IBA1, CD44, and GAPDH) in tri-cultures. See also Figure S5O for monocultures.
(C and D) ELISA measurements of secreted CLU and APOE in tri-cultures, normalized to total protein.
(E) Representative WB of phosphorylated tau (pTAU and PS214), total tau, and GAPDH in tri-cultures.
(F–H) Quantification of pTAU epitopes normalized to total tau. See Figure S6A for pTAU217 and AT8 blots. See Figure S6B for total tau quantifications.
(I) Representative immunostaining of neuron-astrocyte co-cultures: TUJ1 (neurons, gray) and CD44 (astrocytes, red). Scale bar, 100 μM.
(J) ELISA measurement of secreted CLU in co-cultures, normalized to total protein.
(K) pTAU quantification in co-cultures, normalized to total tau. See Figure S6C for representative WB.
(L) ELISA measurement of secreted APOE in co-cultures, normalized to total protein.
(M) Microglia clusters from scRNA-seq of tri-cultures, defined by marker expression. See Figure S7 for all clusters generated across tri-culture conditions.
(N) Dot plot of representative DEGs between cell groups (Wilcoxon rank sum test, FDR $p < 0.05$, except TREM2, FDR $p = 0.11$). See Table S5.
(O) ELISA measurement of C1q in tri-cultures, normalized to IBA1.
Data shown as mean ± SEM, normalized to WT co-cultures. $N = 2$ genetic backgrounds, 4 differentiations, and 3 wells per differentiation. Two-way ANOVA with Sidak's multiple comparisons test, $^{****}p < 0.0001$, $^{***}p < 0.001$, $^{**}p < 0.01$, $^{*}p < 0.05$; ns, not significant.

Please cite this article in press as: Lish et al., CLU alleviates Alzheimer's disease-relevant processes by modulating astrocyte reactivity and microglia-dependent synaptic density, Neuron (2025), https://doi.org/10.1016/j.neuron.2025.03.034

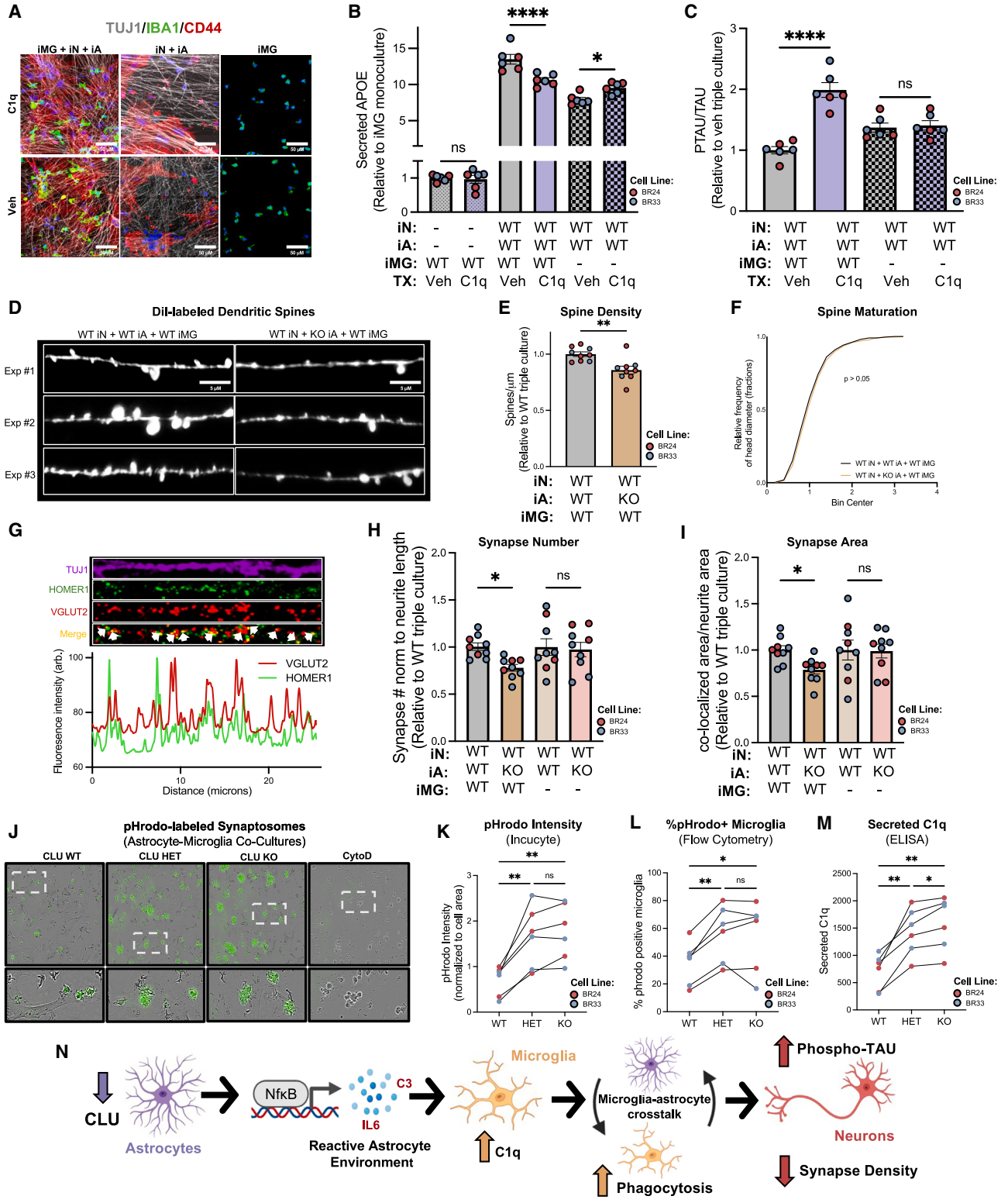

Figure 5. Microglia-dependent decreases in synapse density in neurons co-cultured with CLU-deficient astrocytes

(A) Immunostaining of microglia-astrocyte-neuron, astrocyte-neuron, and microglia cultures treated with vehicle or C1q (400 ng/mL, 72 h). TUJ1 (neurons, gray), CD44 (astrocytes, red), and IBA1 (microglia, green). Scale bar, 50 µM.

(B) ELISA measurement of secreted APOE across culture conditions, normalized to microglia monoculture.

(legend continued on next page)

[UCI]; Milinkeviciute et al., unpublished [Figure 6A]). Mice carrying the *CLU* risk SNP exhibited reduced CLU protein levels (Figures 6B–6E), consistent with our findings in *postmortem* human brains (Figures 1H–1J). Bulk RNA-seq of hippocampal tissue revealed significant overlap in dysregulated pathways between *CLU* risk SNP mice and CLU-deficient astrocytes (Figures 6F and 6G; Table S6). Notably, genes linked to inflammation (*Cd68*, *Icam1*, *Itgb1*, *Mdk*, and *Tnfrsf1b*), complement activation (*C1qa*, *C1ab*, *C1qc*, *C3*, and *C3ar1*), and phagocytosis (*Axl*, *Clec7a*, *Trem2*, *Itgam*, and *Tyrobp*) were upregulated in mice carrying the risk allele (Figures 6H and 6I; Table S6). These findings suggest that reduced CLU levels in an AD mouse model carrying the *CLU* risk allele are associated with complement signaling and phagocytosis dysfunction.

Our analysis of human *postmortem* brain tissue revealed the strongest associations between decreased CLU expression and *CLU* risk alleles in individuals with a high neuropathological burden (Figure 1I), suggesting protective alleles may enhance CLU upregulation over time. To explore this, we analyzed longitudinal plasma samples from individuals with varying CLU genotypes and AD diagnoses using the NUcleic acid Linked Immuno-Sandwich Assay (NULISA assay),[79] which includes 120 neurodegeneration-associated proteins and Meso Scale Discovery (MSD) ELISA (Figures 7A and 7B; Table S7). Linear regression across CLU SNP dosage showed that CLU genotype significantly associated with changes in CLU, C-reactive protein (CRP), cystatin C (CST3), and IL-6 levels over time (Figure 7C). Protective alleles correlated with greater CLU increases (Figures 7D–7F), while risk alleles were linked to elevated IL-6, CST3, and CRP (Figures 7G–7I). These inflammatory markers were also elevated in CLU HET and/or KO astrocytes in at least one genetic background (Figures 2H and S4C; Table S3), reinforcing the link between *CLU* genotype, expression, and inflammation.

Finally, we leveraged the ROSMAP iPSC cohort[56,80] to examine the functional effects of *CLU* risk and protective alleles in human cell-based models. Given that CLU expression differences were most pronounced under high neuropathological burden and the importance of microglia in regulating aspects of CLU's function, we tested these alleles in an AD-relevant tri-culture system (Figure 8A). We combined neurons with fAD mutations (*APPSwe; PSEN1M146V*), *APOE4/4* microglia, and astrocytes homozygous for either *CLU* rs11787077 protective (T) or risk (C) alleles (14 lines total, all *APOE3/3*). After culture establishment, we assessed AD-related pathology, including Aβ measures, tau phosphorylation, and the expression of proteins previously identified as dysregulated in CLU KO vs. WT conditions (Figures 8B–8H and S8A–S8I; Table S8). Remarkably, tri-cultures with protective *CLU* alleles exhibited significantly higher CLU and APOE levels, reduced C3, and decreased phosphorylated tau (202/205 and 214). Across the 14 lines, CLU protein levels were positively correlated with APOE and inversely with C3, C1q, and phosphorylated tau (Figures 8I, 8J, and S8J). To explore functional outcomes at the synaptic level, we measured spine density using DiI labeling. While grouping by *CLU* genotype alone showed no significant difference (Figure S8G), higher CLU levels correlated with increased spine density, while elevated C3 secretion was associated with reduced spine density (Figures 8I–8K and S8J). Importantly, not all genetic backgrounds with *CLU* protective alleles exhibited these effects, presenting an opportunity for future research to identify additional genetic factors that may influence the effectiveness of these alleles in modulating immune processes. Taken together, these analyses across multiple experimental modalities provide compelling evidence that AD-associated variants at the *CLU* locus influence CLU expression, inflammatory and complement-mediated responses, and tau phosphorylation.

DISCUSSION

The connection between CLU and AD was first identified nearly three decades ago when elevated CLU protein levels were observed in AD brains. However, its role in AD remains unresolved. Early studies have suggested that CLU plays a neuroprotective role by inhibiting Aβ aggregation,[63,65,66] and that elevated plasma levels correlate with slower brain atrophy.[6,81,82] However, seemingly contradictory findings report that increased CLU in cerebrospinal fluid was associated with greater entorhinal cortex

(C) Quantification of phosphorylated tau across conditions with vehicle or C1q. See Figure S6D for representative WB.
(D) Representative DiI-stained dendritic spines in tri-cultures. Scale bar, 5 μM.
(E) Spine density measurements, blinded analysis. $N = 2$ genetic backgrounds, 3 differentiations, and 3 wells per differentiation. Unpaired Student's t test (two-tailed), $^{**}p < 0.01$.
(F) Cumulative distribution of spine head diameters (Kolmogorov-Smirnov test).
(G) Representative neurite labeled with TUJ1, HOMER1, VGLUT2, and colocalized HOMER1-VGLUT2 puncta (80% overlap). Arrows indicate synaptic structures. Intensity plot for VGLUT2 (red) and HOMER1 (green) along a 25 μm region.
(H and I) Quantification of colocalized HOMER1-VGLUT2 area and puncta, normalized to neurite area. $N = 2$ genetic backgrounds, 3 differentiations, and 3 wells per differentiation. Two-way ANOVA with Sidak's test, $^{*}p < 0.05$; ns, not significant.
(J) Representative images of astrocyte-microglia co-cultures treated with pHrodo-488/fluorescein isothiocyanate (FITC)-labeled synaptosomes, cytochalasin D used as a negative control.
(K and L) Quantification of synaptosome phagocytosis by (K) Incucyte live-cell imaging and (L) flow cytometry. Phagocytosis represented by FITC/pHrodo intensity.
(M) ELISA measurement of C1q levels in culture media corresponding to (K) and (L). All data presented as mean ± SEM.
For (K–M), $N = 2$ genetic backgrounds, 6 differentiations, and 3 wells per differentiation. Each dot represents the average of 3 technical replicates. RM one-way ANOVA, $^{**}p < 0.01$, $^{*}p < 0.05$; ns, not significant. All data presented as mean ± SEM.
(N) Schematic model summarizing results, relaying that CLU deficiency in astrocytes elevates baseline NF-κB signaling, promoting a reactive astrocyte-like state with elevated extracellular levels of C3 and IL-6. In tri-cultures, CLU-deficient astrocytes are associated with increased microglia C1q section and phagocytosis, coinciding with elevated phosphorylated tau and synapse loss in neurons.
See also Table S5.

Please cite this article in press as: Lish et al., CLU alleviates Alzheimer's disease-relevant processes by modulating astrocyte reactivity and microglia-dependent synaptic density, Neuron (2025), https://doi.org/10.1016/j.neuron.2025.03.034

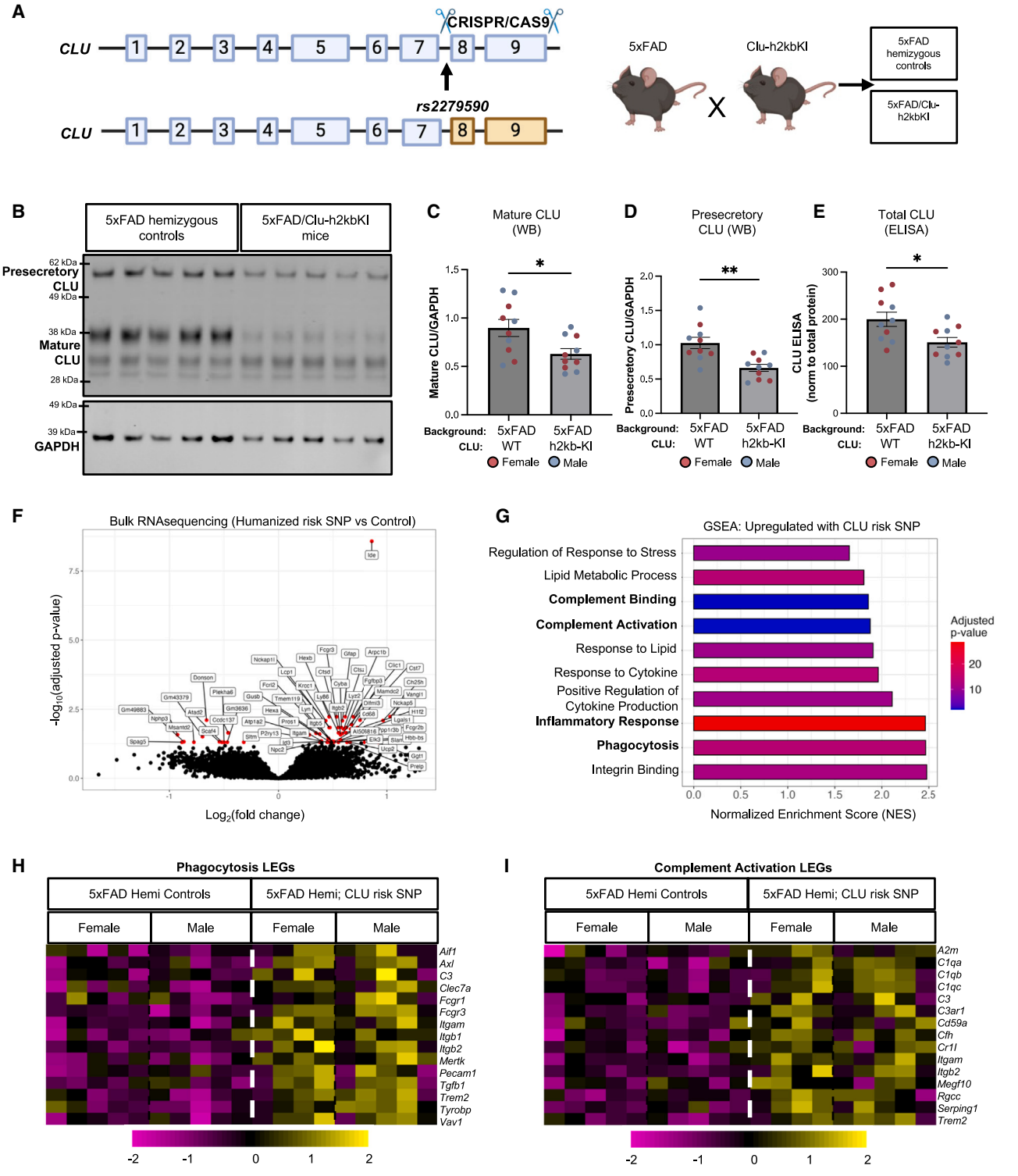

Figure 6. Humanized *CLU* risk SNP mice show reduced CLU expression and elevated complement and phagocytosis pathways in 5× FAD mice

(A) Schematic of CRISPR editing strategy. A 2 kb human CLU region (intron 7–exon 9), including the AD-risk rs2279590 variant, was inserted into the *CLU* locus in C57BL/6J mice. Clu-h2kb-KI mice were crossed with 5xFAD mice and aged to 4 months.

(B) Representative WB of cerebral cortical tissue from 5×FAD controls and 5×FAD/Clu-h2kb-KI mice, probed for CLU and GAPDH.

(legend continued on next page)

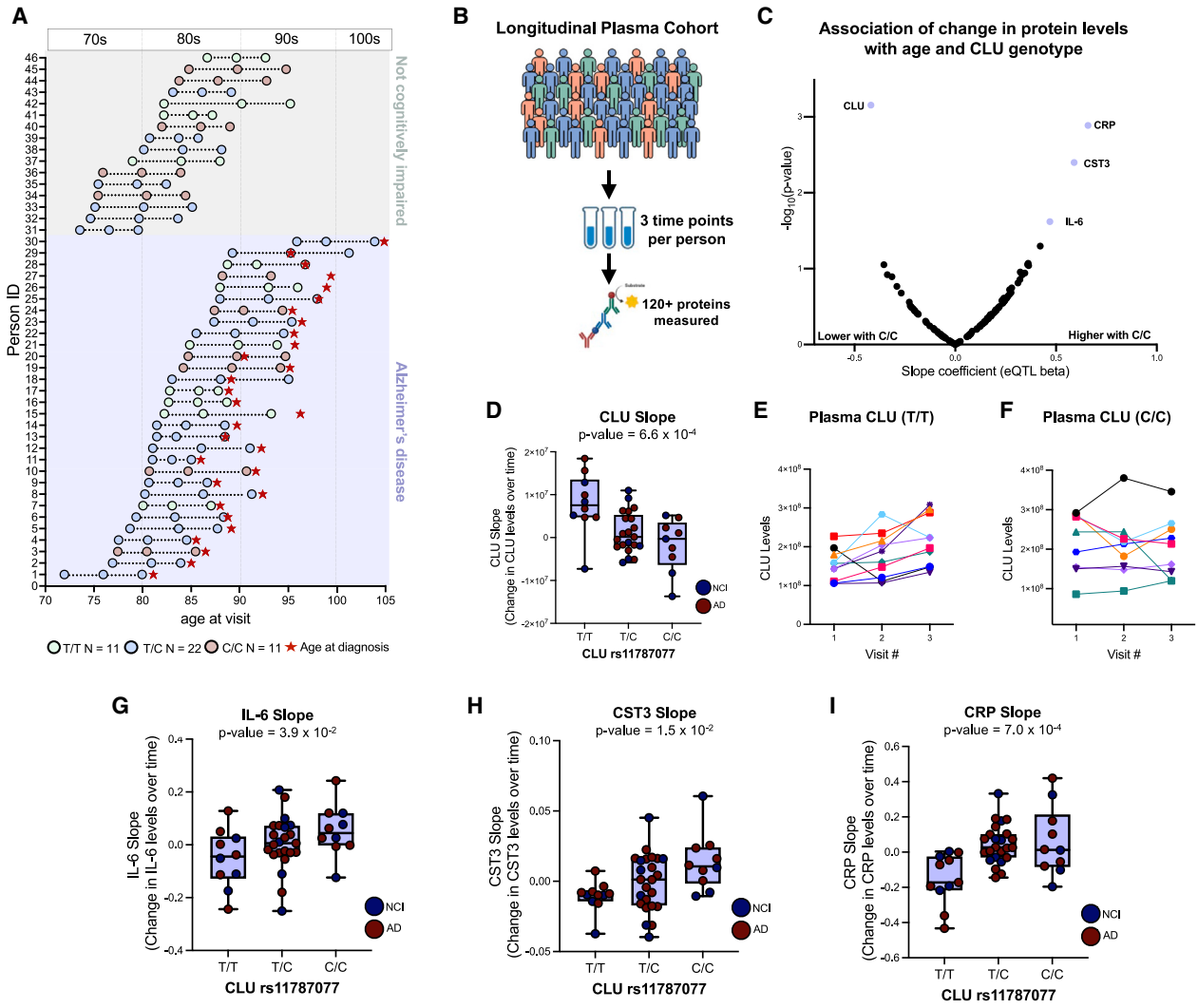

Figure 7. Protective *CLU* alleles enhance CLU upregulation and reduce inflammatory profiles in human plasma

(A and B) Overview of the longitudinal ROSMAP plasma cohort analyzed. The plot shows ages at each plasma collection analyzed (three per person). Individuals are color-coded by *CLU* rs11787077 genotype: T/T (green, $N = 11$), T/C (blue, $N = 24$), and C/C (red, $N = 11$). Red stars indicate the age of first clinical AD diagnosis.

(C) Simple linear regression analysis of protein slopes across *CLU* SNP rs11787077 dosage.

(D and G–I) Slopes of CLU (D), IL-6 (G), CST3 (H), and CRP (I) by *CLU* rs11787077 genotype with simple linear regression *p* values.

(E and F) Plasma CLU levels at each visit for individuals with T/T (E) and C/C (F) *CLU* rs11787077 genotypes.

For all graphs, data are presented as mean values ± SEM.

See also Table S7.

atrophy,[83] and studies in AD mouse models show mixed results. Some studies associate CLU deficiency with reduced Aβ deposits,[84] while others suggest CLU reduction exacerbates amyloid pathology.[85] To clarify CLU's role in the aging brain, we systematically analyzed CLU expression and function across hundreds of deeply phenotyped aged human participants, a mouse model carrying a humanized *CLU* risk variant, and human cellular models of CLU deficiency and LOAD risk variants. Our findings collectively support a protective role for CLU in the aging brain and AD. Analyses of brain tissue from over

(C–E) Quantification of mature CLU (C), presecretory CLU (D), and total CLU (E, ELISA). $N = 5$ females and 5 males per genotype. Unpaired Student's t test (two-tailed), $^{**}p < 0.01$ and $^{*}p < 0.05$. Data presented as mean ± SEM.

(F) Bulk RNA-seq was performed on hippocampal tissue on $N = 19$ mice; nine 5×FAD hemi;CLU (4 females and 5 males) and 10 5×FAD controls (5 females and 5 males). Volcano plot of DEGs (5×FAD/Clu-h2kb-KI vs. 5×FAD). Red, *p*adj. < 0.05. See Table S6.

(G) Gene set enrichment analysis results from differential gene expression analysis. See Table S6.

(H and I) Heatmap of expression of leading-edge genes for phagocytosis (H) and complement activation (I) upregulated in 5×FAD/Clu-h2kb-KI.

Please cite this article in press as: Lish et al., CLU alleviates Alzheimer's disease-relevant processes by modulating astrocyte reactivity and microglia-dependent synaptic density, Neuron (2025), https://doi.org/10.1016/j.neuron.2025.03.034

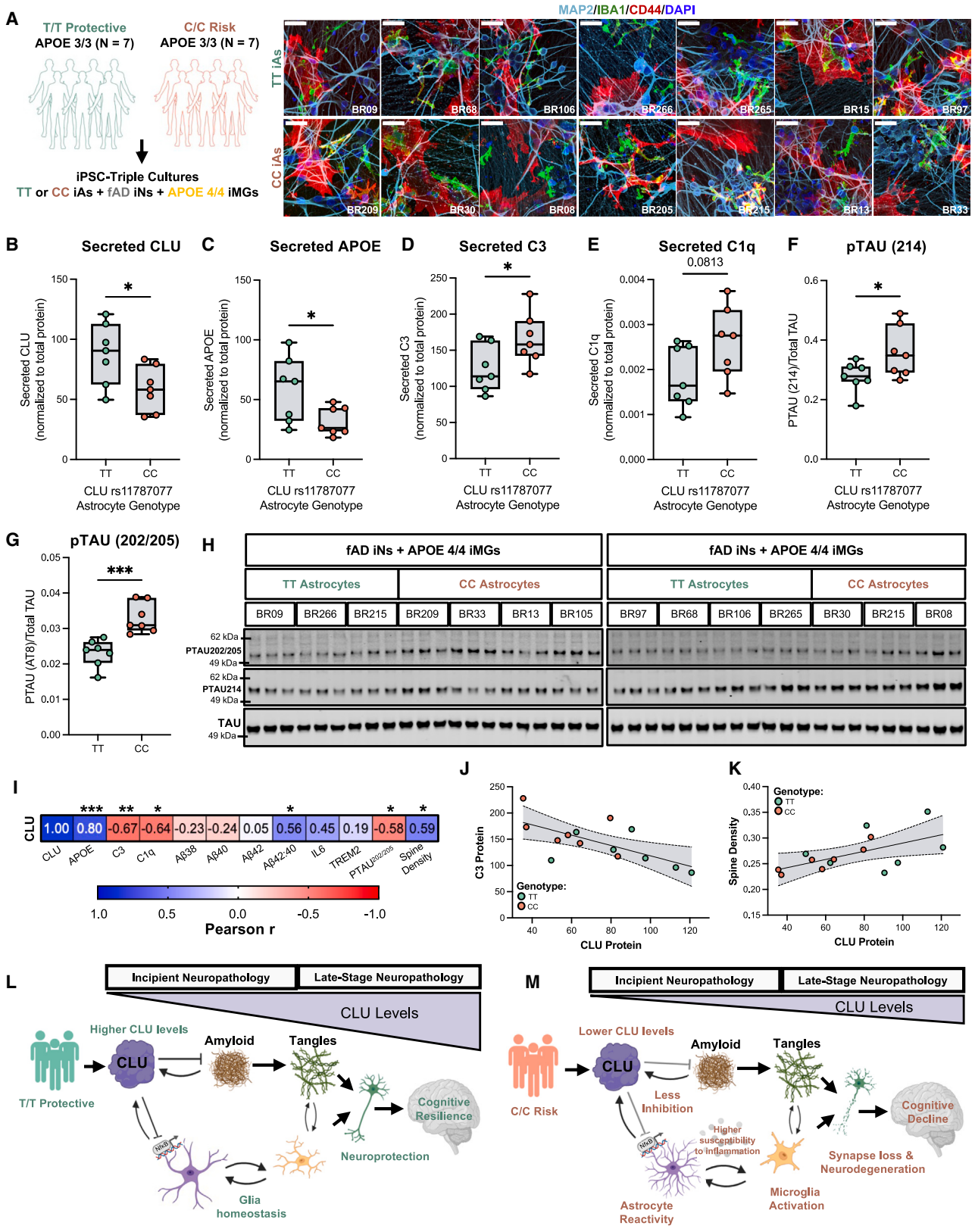

(legend on next page)

Please cite this article in press as: Lish et al., CLU alleviates Alzheimer's disease-relevant processes by modulating astrocyte reactivity and microglia-dependent synaptic density, Neuron (2025), https://doi.org/10.1016/j.neuron.2025.03.034

700 participants[50] in the ROSMAP studies showed that, while CLU protein levels are elevated in AD, individuals carrying the risk allele of the leading *CLU* AD-associated SNP (rs11787077) exhibited reduced CLU upregulation in response to accumulated neuropathology (Figure 1I). This pattern was evident in plasma, where CLU levels increased over time in individuals with protective alleles but remained unchanged in those with *CLU* risk alleles (Figures 7D–7F). Similarly, a humanized mouse model and iAs carrying *CLU* risk SNPs exhibited lower CLU levels under high neuropathological burden (Figures 6B–6E and 8B).

Aβ plaques and tau tangles are hallmark AD pathologies, but tau pathology and synapse loss correlate more strongly with cognitive impairment.[86,87] We observed a strong negative correlation between tangle score and global cognition in individuals with CLU risk alleles (Figures 1K and 1L), but this relationship was strikingly absent in those with two protective CLU alleles (Figure 1M), suggesting protective alleles may mitigate tau-related cognitive decline. Previous studies in a P301L tauopathy mouse model showed that CLU loss exacerbates tau pathology.[67] Building on this, our iPSC-based findings reveal that microglia are necessary for phosphorylated tau accumulation in neurons co-cultured with CLU-deficient astrocytes. Notably, *CLU* risk alleles in astrocytes also increased phosphorylated tau in co-cultured neurons (Figures 8F and 8G), linking astrocytic CLU genetics to tau pathology. While it is unclear whether CLU directly interacts with tau in our cellular model, as suggested by studies in mice,[67] C1q treatment increased phosphorylated tau levels only in the presence of microglia (Figure 5C). Recent research suggests that microglial C1q may be internalized by neurons and interact with ribonucleoprotein complexes,[88] with RNA-binding proteins co-localizing with phosphorylated tau.[89,90] These findings warrant further studies to explore C1q's potential role in tau pathology and whether it mediates CLU's effect on tau.

A major strength of this study is the consistency of phenotypes across experimental models, while also reinforcing prior findings from mouse studies of CLU function. A recurrent theme across our approaches is the upregulation of inflammatory proteins in CLU-deficient conditions. Our proteomics analysis in CLU KO versus WT cell models revealed that CLU loss increases human astrocyte reactivity, even in the absence of external inflammatory stimuli or AD-related insults like Aβ or tau. Mechanistically, we found that chronic CLU deficiency in astrocytes enhances NF-κB signaling, consistent with mouse and immortalized cell line studies showing that CLU inhibits NF-κB activity by binding and sequestering phosphorylated IκBα.[29–32] Additionally, previous studies have shown that CLU regulates complement activity by binding C5b-9 to form an inactive complex.[91–95] Here, we show that CLU deficiency elevated complement proteins C3 in astrocytes and C1q in microglia (Figures 2I and 4O), suggesting that CLU regulates multiple components of the complement pathway beyond what was previously recognized. Notably, CLU overexpression and NF-κB inhibition rescued C3 upregulation in CLU HET and KO iAs (Figures 3C and 3F), mirroring earlier work identifying C3 as an astroglial target of NF-κB in mice.[60]

Beyond loss-of-function models, our studies of LOAD-associated variants at the *CLU* locus consistently associate risk variants with reduced CLU levels with heightened inflammatory responses. Mice carrying a human risk variant exhibited lower CLU protein levels and increased activation of inflammation, complement, and phagocytosis pathways (Figure 6B–6I). Similarly, in a cohort of longitudinal plasma samples, individuals with protective alleles displayed higher CLU levels over time, while those with risk alleles exhibited increased IL-6, CRP, and CST3 with aging (Figure 7D–7I). Remarkably, these same inflammatory proteins were upregulated in CLU-deficient astrocytes (Figures 2H and S4C; Table S3). The association between plasma CLU changes with age and genotype is compelling, especially in light of recent studies showing that plasma CLU, upregulated during exercise, can cross the blood-brain barrier to suppress inflammatory signaling in brain endothelial cells.[96] Since CLU levels in the plasma are strongly influenced by hepatocyte production, it is plausible that factors like exercise could drive hepatic changes in CLU and inflammatory protein expression to varying degrees with CLU genotype, which could in turn affect brain health. Additionally, tri-cultures with astrocytes carrying *CLU* risk alleles also showed reduced CLU levels and elevated complement proteins (Figures 8B, 8D, and S8E), mirroring CLU loss-of-function models. Together, these results suggest that *CLU* genetic variants modulate both CLU expression

Figure 8. *CLU* risk alleles in genetically diverse iPSC-derived tri-cultures recapitulate CLU loss-of-function phenotypes

(A) Overview of experimental design. Astrocytes derived from fourteen iPSC lines from the ROSMAP study, seven homozygous for the CLU protective allele (T) and seven for the risk allele (C), were co-cultured with *APOE 4/4* microglia and neurons carrying familial AD mutations. Immunostaining of co-cultures with MAP2 (cyan), CD44 (red), and IBA1 (green). Scale bar, 30 μM.

(B–E) ELISA measurements of secreted CLU, APOE, C3, and C1q in tri-cultures, stratified by astrocyte *CLU* genotype. Each dot represents astrocytes from a unique iPSC line, averaged across three replicates. See Figures S8A–S8I.

(F and G) Quantification of phosphorylated tau, normalized to total tau in tri-cultures, stratified by astrocyte genotype. Each dot represents a unique astrocyte line, averaged across three replicates.

(H) Representative WB of phosphorylated tau (202/205 and 214) and total tau in tri-cultures. See Figure S8I for pTAU 217.

For all graphs, data are presented as mean values ± SEM. Unpaired Student's t test (two-tailed), $^{***}p < 0.001$ and $^{*}p < 0.05$.

(I) Pearson correlations of secreted CLU with other secreted proteins, pTAU, and spine density across co-cultures. See Figure S8J.

(J and K) Correlation of CLU protein with C3 (J) or spine density (K) in *CLU* CC and TT tri-cultures. Shaded area indicates 95% confidence interval.

(L) Model of CLU-mediated protection in Alzheimer's dementia. Our findings, along with CLU's established role as an Aβ molecular chaperone, suggest that CLU is upregulated in individuals with protective alleles as amyloid and tau neuropathology accumulates. This upregulation may help mitigate microglia-astrocyte-driven inflammation, preserving synaptic integrity and cognitive function.

(M) Model of how *CLU* risk SNPs may influence disease progression. Risk alleles at the *CLU* locus are linked to reduced CLU expression in astrocytes, weakening its ability to inhibit complement and NF-κB signaling. This deficiency may increase susceptibility to inflammation, accelerate synapse loss, and heighten the risk of cognitive decline.

See also Table S8.

Please cite this article in press as: Lish et al., CLU alleviates Alzheimer's disease-relevant processes by modulating astrocyte reactivity and microglia-dependent synaptic density, Neuron (2025), https://doi.org/10.1016/j.neuron.2025.03.034

and inflammatory/complement-mediated responses, shedding new light on decades of research positing a functional role for CLU in suppressing immune processes. Coupled with CLU's well-characterized ability to inhibit Aβ aggregation,[63,65,66] our findings indicate that protective *CLU* alleles promote the upregulation of CLU to counteract accumulating amyloid and tau, thereby mitigating inflammatory interactions between microglia and astrocytes (Figure 8L). In contrast, reduced CLU levels—influenced by genetic variants associated with AD—may impair these protective effects and increase susceptibility to disease (Figure 8M).

At the genetic level, *CLU* risk variants may influence cellular processes by modulating *CLU* expression through chromatin regulation. Although our analyses of human brain and iPSC models primarily focus on rs11787077 for visualization of results, this SNP—as well as many other LOAD-associated *CLU* variants located in intronic regions (Figure S1D)—are in high linkage disequilibrium ($R^2 > 90\%$; Figure 1J). These variants may affect gene expression via shared regulatory mechanisms rather than through direct coding alterations (although our data cannot rule out the impact of a specific nucleotide change resulting from one of the LOAD-associated SNPs). Because chromatin states and regulatory interactions can be governed by clusters of linked genetic variants, altering a lone SNP in an isogenic iPSC model may not fully capture the broader genomic context of *CLU* risk. This underscores the value of using iPSCs derived from large cohorts like ROSMAP that provides a physiologically relevant framework for studying endogenous *CLU* risk and protective haplotypes. Future research should aim to delineate the regulatory architecture of the *CLU* locus to elucidate how these risk variants collectively influence CLU expression and function in AD.

CLU genetic variants may influence synaptic integrity by modulating CLU expression. Mouse studies have previously shown that astrocytic CLU loss impairs presynaptic function and reduces spine density.[25] Extending this to a human genomic context, we uncover a key role for microglia in this process. While the precise mechanism linking microglia-dependent regulation of astrocyte CLU to reduced synaptic density remains to be determined, our findings offer valuable insights. Given that CLU deficiency results in elevated levels of C3 and C1q (Figures 2I and 4O) and increased microglia phagocytosis (Figures 5K and 5L), it is tempting to speculate that the CLU-dependent reduction of synaptic density (Figures 5D–5I) is due to complement-mediated synaptic pruning by microglia. Supporting this, C1q administration to tri-cultures phenocopies the loss of CLU, lowering TREM2 and APOE levels and increasing phosphorylated tau (Figures 5A–5C and S6G–S6J). Intriguingly, both APOE and TREM2, which are dysregulated under CLU-deficient conditions, modulate the complement cascade via C1q binding,[73,97] and TREM2 in microglia is proposed to be a receptor for both APOE and CLU.[72] Deficiencies in APOE or TREM2 impair synaptic pruning,[98–100] and CLU has been shown to accumulate at synapses in human AD brain tissue, more prominently in *APOE4* carriers.[24] However, TREM2 alterations in our study were less consistent than changes in C1q or APOE, suggesting that regulation of its levels may not be the central feature of its relationship with CLU. Moving forward, modulating TREM2, APOE, or C1q in microglia will be an important strategy to clarify the dependency of these proteins on CLU-mediated synapse integrity and other phenotypes detailed herein.

Limitations of the study

While *postmortem* brain analyses are highly valuable, they are limited to a single time point for each individual. Although our study includes longitudinal plasma samples, the small cohort size (46 individuals) and the variability in age and collection timing complicate interpretation. Future studies with additional cohorts and time points would be useful to expand upon these observations. It is important to recognize that *CLU* SNPs have a small effect size on LOAD risk, making it unsurprising that associations between *CLU* risk variants and protein levels in human tissues—derived from individuals with diverse ages, sexes, ancestries, co-pathologies, and environmental exposures—are modest. CLU expression is also modulated by other factors, such as physical aerobic exercise,[96] aging,[101] and diabetes,[102] which may contribute to the heterogeneity observed in human cohort studies and discrepancies reported across studies. While our tri-culture model enables the study of neuron-glial interactions, it has inherent limitations, such as the lack of AD-related factors such as aging and differences in expression profiles, cellular ratios, and brain region diversity of cell types. Nevertheless, our findings will open new avenues for targeted investigations into the molecular mechanisms by which CLU regulates intercellular communication between glia and neurons in disease risk and resilience.

RESOURCE AVAILABILITY

Lead contact

Requests for further information and resources should be directed to the lead contact, Tracy Young-Pearse (tpearse@bwh.harvard.edu).

Materials availability

All unique/stable reagents generated in this study are available from the lead contact with a completed materials transfer agreement (MTA). ROSMAP iPSC lines are available from the New York Stem Cell Foundation through the NYSCF Repository (repository@nyscf.org) with completed MTA to obtain cohort data and samples (radc.rush.edu).

Data and code availability

- Mouse data: Bulk RNA sequencing data (https://adknowledgeportal.synapse.org) (https://adknowledgeportal.org/DataAccess/Instructions) have been deposited in the Gene Expression (GEO) database, with accession number GEO: GSE294133.
- Cell data: scRNA-seq data have been deposited in the Gene Expression (GEO) database, with accession number GEO: GSE289565. TMT-MS data have been deposited to the Synapse database, with accession numbers Synapse: syn52502746, Synapse: syn50208824, and Synapse: syn53190960.
- Any additional information required to reanalyze the data reported in this paper is available from the lead contact upon request.
- For quick visualization of datasets generated in this study, please also see https://youngpearselab.shinyapps.io/clu_ia/.

ACKNOWLEDGMENTS

We thank the AMP-AD consortium for feedback and data sharing (see "data and code availability"), the NeuroTechnology Studio at Brigham and Women's

Hospital for access to microscopy equipment and consultation, the iPSC NeuroHub at Brigham and Women's Hospital for technical support, the Proteomics Core at Emory University for analysis and consultation, and Maria Lehtinen, Vik Khurana, and Lee Rubin for Dissertation Advisory Committee guidance. Thanks to the Young-Pearse lab members and to Gizem Terzioglu and Lilia Sattler for synaptosome preparation. We acknowledge the Chao Family Comprehensive Cancer Center Transgenic Mouse Facility Shared Resource at UCI (P30CA062203). This study was supported by the MODEL-AD consortium (U54AG054349); the National Science Foundation Graduate Research Fellowship (1745303); and NIH grants U01AG061356, RF1AG 057473, U01AG046152, R01AG066831, RF1AG072167, U01AG072572, R01NS117446, and R01AG055909. ROSMAP is supported by P30AG10161, P30AG72975, R01AG15819, R01AG17917, U01AG46152, and U01AG61356. This work also was supported by an Alzheimer's Association Zenith Award (T.L.Y.-P.). Scientific illustrations in this work incorporate elements adapted from BioRender. The results published here are in part based on data obtained from the AD Knowledge Portal (https://adknowledgeportal.org).

AUTHOR CONTRIBUTIONS

Conceptualization, A.M.L. and T.L.Y.-P.; methodology, A.M.L., S.E.H., R.V.P., S.B.F., and T.L.Y.-P.; software, A.M.L., R.V.P., V.M., and T.L.; validation, A.M.L., G.A.O, S.E.H., K.D.A., P.C.G., M.F., and E.F.L.G.; formal analysis, A.M.L., R.V.P., T.L., C.R.B., and T.L.Y.-P.; investigation, A.M.L., S.E.H., E.F.L.G., T.L., A.M.S., C.R.B., K.N.G., G.M., and K.D.A.; resources, T.L.Y.-P.; data curation, A.M.L., R.V.P, and T.L.Y.-P.; writing—original draft, A.M.L. and T.L.Y.-P.; writing—review and editing, A.M.L., R.V.P., E.F.LG., S.E.H, C.R.B., K.D.A., T.L., A.M.S., N.T.S., D.A.B., and T.L.Y.-P.; visualization, A.M.L., R.V.P., C.R.B., T.L., and T.L.Y.-P.; supervision, T.L.Y.-P.; project administration, T.L.Y.-P. and D.A.B.; funding acquisition T.L.Y.-P., A.M.L., D.A.B., P.L.D.J., and V.M.

DECLARATION OF INTERESTS

The authors declare no competing interests.

STAR★METHODS

Detailed methods are provided in the online version of this paper and include the following:

SUPPLEMENTAL INFORMATION

Supplemental information can be found online at https://doi.org/10.1016/j.neuron.2025.03.034.

Received: August 21, 2024
Revised: February 25, 2025
Accepted: March 31, 2025
Published: April 30, 2025

REFERENCES

1. Bertrand, P., Poirier, J., Oda, T., Finch, C.E., and Pasinetti, G.M. (1995). Association of apolipoprotein E genotype with brain levels of apolipoprotein E and apolipoprotein J (clusterin) in Alzheimer disease. Brain Res. Mol. Brain Res. *33*, 174–178. https://doi.org/10.1016/0169-328x(95)00097-c.
2. Lidström, A.M., Bogdanovic, N., Hesse, C., Volkman, I., Davidsson, P., and Blennow, K. (1998). Clusterin (apolipoprotein J) protein levels are increased in hippocampus and in frontal cortex in Alzheimer's disease. Exp. Neurol. *154*, 511–521. https://doi.org/10.1006/exnr.1998.6892.
3. May, P.C., Lampert-Etchells, M., Johnson, S.A., Poirier, J., Masters, J.N., and Finch, C.E. (1990). Dynamics of gene expression for a hippocampal glycoprotein elevated in Alzheimer's disease and in response to experimental lesions in rat. Neuron *5*, 831–839. https://doi.org/10.1016/0896-6273(90)90342-d.
4. Miners, J.S., Clarke, P., and Love, S. (2017). Clusterin levels are increased in Alzheimer's disease and influence the regional distribution of Aβ. Brain Pathol. *27*, 305–313. https://doi.org/10.1111/bpa.12392.
5. Duguid, J.R., Bohmont, C.W., Liu, N.G., and Tourtellotte, W.W. (1989). Changes in brain gene expression shared by scrapie and Alzheimer disease. Proc. Natl. Acad. Sci. USA *86*, 7260–7264. https://doi.org/10.1073/pnas.86.18.7260.
6. May, P.C., Johnson, S.A., Poirier, J., Lampert-Etchells, M., and Finch, C.E. (1989). Altered gene expression in Alzheimer's disease brain tissue. Can. J. Neurol. Sci. *16*, 473–476. https://doi.org/10.1017/s0317167100029796.
7. Harold, D., Abraham, R., Hollingworth, P., Sims, R., Gerrish, A., Hamshere, M.L., Pahwa, J.S., Moskvina, V., Dowzell, K., Williams, A., et al. (2009). Genome-wide association study identifies variants at CLU and PICALM associated with Alzheimer's disease. Nat. Genet. *41*, 1088–1093. https://doi.org/10.1038/ng.440.
8. Bellenguez, C., Küçükali, F., Jansen, I.E., Kleineidam, L., Moreno-Grau, S., Amin, N., Naj, A.C., Campos-Martin, R., Grenier-Boley, B., Andrade, V., et al. (2022). New insights into the genetic etiology of Alzheimer's disease and related dementias. Nat. Genet. *54*, 412–436. https://doi.org/10.1038/s41588-022-01024-z.
9. Roussotte, F.F., Gutman, B.A., Madsen, S.K., Colby, J.B., and Thompson, P.M.; Alzheimer's Disease Neuroimaging Initiative (2014). Combined effects of Alzheimer risk variants in the CLU and ApoE genes on ventricular expansion patterns in the elderly. J. Neurosci. *34*, 6537–6545. https://doi.org/10.1523/JNEUROSCI.5236-13.2014.
10. Ling, I.-F., Bhongsatiern, J., Simpson, J.F., Fardo, D.W., and Estus, S. (2012). Genetics of clusterin isoform expression and Alzheimer's disease

risk. PLoS One *7*, e33923. https://doi.org/10.1371/journal.pone.0033923.

11. Tan, L., Wang, H.-F., Tan, M.-S., Tan, C.-C., Zhu, X.-C., Miao, D., Yu, W.-J., Jiang, T., Tan, L., Yu, J.-T., et al. (2016). Effect of CLU genetic variants on cerebrospinal fluid and neuroimaging markers in healthy, mild cognitive impairment and Alzheimer's disease cohorts. Sci. Rep. *6*, 26027. https://doi.org/10.1038/srep26027.
12. Allen, M., Zou, F., Chai, H.S., Younkin, C.S., Crook, J., Pankratz, V.S., Carrasquillo, M.M., Rowley, C.N., Nair, A.A., Middha, S., et al. (2012). Novel late-onset Alzheimer disease loci variants associate with brain gene expression. Neurology *79*, 221–228. https://doi.org/10.1212/WNL.0b013e3182605801.
13. Padhy, B., Nanda, G.G., Chowdhury, M., Padhi, D., Rao, A., and Alone, D.P. (2014). Role of an extracellular chaperone, Clusterin in the pathogenesis of Pseudoexfoliation Syndrome and Pseudoexfoliation Glaucoma. Exp. Eye Res. *127*, 69–76. https://doi.org/10.1016/j.exer.2014.07.005.
14. Padhy, B., Hayat, B., Nanda, G.G., Mohanty, P.P., and Alone, D.P. (2017). Pseudoexfoliation and Alzheimer's associated CLU risk variant, rs2279590, lies within an enhancer element and regulates CLU, EPHX2 and PTK2B gene expression. Hum. Mol. Genet. *26*, 4519–4529. https://doi.org/10.1093/hmg/ddx329.
15. Szymanski, M., Wang, R., Bassett, S.S., and Avramopoulos, D. (2011). Alzheimer's risk variants in the clusterin gene are associated with alternative splicing. Transl. Psychiatry *1*, e18. https://doi.org/10.1038/tp.2011.17.
16. Liu, Z., Chao, J., Wang, C., Sun, G., Roeth, D., Liu, W., Chen, X., Li, L., Tian, E., Feng, L., et al. (2023). Astrocytic response mediated by the CLU risk allele inhibits OPC proliferation and myelination in a human iPSC model. Cell Rep. *42*, 112841. https://doi.org/10.1016/j.celrep.2023.112841.
17. Kida, E., Choi-Miura, N.H., and Wisniewski, K.E. (1995). Deposition of apolipoproteins E and J in senile plaques is topographically determined in both Alzheimer's disease and Down's syndrome brain. Brain Res. *685*, 211–216. https://doi.org/10.1016/0006-8993(95)00482-6.
18. Camacho, J., Moliné, T., Bonaterra-Pastra, A., Ramón Y Cajal, S., Martínez-Sáez, E., and Hernández-Guillamon, M. (2019). Brain ApoA-I, ApoJ and ApoE Immunodetection in Cerebral Amyloid Angiopathy. Front. Neurol. *10*, 187. https://doi.org/10.3389/fneur.2019.00187.
19. McGeer, P.L., Kawamata, T., and Walker, D.G. (1992). Distribution of clusterin in Alzheimer brain tissue. Brain Res. *579*, 337–341. https://doi.org/10.1016/0006-8993(92)90071-g.
20. Wilson, M.R., and Easterbrook-Smith, S.B. (2000). Clusterin is a secreted mammalian chaperone. Trends Biochem. Sci. *25*, 95–98. https://doi.org/10.1016/s0968-0004(99)01534-0.
21. Narayan, P., Orte, A., Clarke, R.W., Bolognesi, B., Hook, S., Ganzinger, K.A., Meehan, S., Wilson, M.R., Dobson, C.M., and Klenerman, D. (2011). The extracellular chaperone clusterin sequesters oligomeric forms of the amyloid-β(1–40) peptide. Nat. Struct. Mol. Biol. *19*, 79–83. https://doi.org/10.1038/nsmb.2191.
22. Wojtas, A.M., Kang, S.S., Olley, B.M., Gatherer, M., Shinohara, M., Lozano, P.A., Liu, C.-C., Kurti, A., Baker, K.E., Dickson, D.W., et al. (2017). Loss of clusterin shifts amyloid deposition to the cerebrovasculature via disruption of perivascular drainage pathways. Proc. Natl. Acad. Sci. USA *114*, E6962–E6971. https://doi.org/10.1073/pnas.1701137114.
23. DeMattos, R.B., Cirrito, J.R., Parsadanian, M., May, P.C., O'Dell, M.A., Taylor, J.W., Harmony, J.A.K., Aronow, B.J., Bales, K.R., Paul, S.M., et al. (2004). ApoE and clusterin cooperatively suppress Abeta levels and deposition: evidence that ApoE regulates extracellular Abeta metabolism in vivo. Neuron *41*, 193–202. https://doi.org/10.1016/s0896-6273(03)00850-x.
24. Jackson, R.J., Rose, J., Tulloch, J., Henstridge, C., Smith, C., and Spires-Jones, T.L. (2019). Clusterin accumulates in synapses in Alzheimer's disease and is increased in apolipoprotein E4 carriers. Brain Commun. *1*, fcz003. https://doi.org/10.1093/braincomms/fcz003.
25. Chen, F., Swartzlander, D.B., Ghosh, A., Fryer, J.D., Wang, B., and Zheng, H. (2021). Clusterin secreted from astrocyte promotes excitatory synaptic transmission and ameliorates Alzheimer's disease neuropathology. Mol. Neurodegener. *16*, 5. https://doi.org/10.1186/s13024-021-00426-7.
26. Calero, M., Tokuda, T., Rostagno, A., Kumar, A., Zlokovic, B., Frangione, B., and Ghiso, J. (1999). Functional and structural properties of lipid-associated apolipoprotein J (clusterin). Biochem. J. *344*, 375–383. https://doi.org/10.1042/bj3440375.
27. Jenne, D.E., and Tschopp, J. (1989). Molecular structure and functional characterization of a human complement cytolysis inhibitor found in blood and seminal plasma: identity to sulfated glycoprotein 2, a constituent of rat testis fluid. Proc. Natl. Acad. Sci. USA *86*, 7123–7127. https://doi.org/10.1073/pnas.86.18.7123.
28. Grassilli, E., Bettuzzi, S., Monti, D., Ingletti, M.C., Franceschi, C., and Corti, A. (1991). Studies on the relationship between cell proliferation and cell death: opposite patterns of SGP-2 and ornithine decarboxylase mRNA accumulation in PHA-stimulated human lymphocytes. Biochem. Biophys. Res. Commun. *180*, 59–63. https://doi.org/10.1016/s0006-291x(05)81254-9.
29. Santilli, G., Aronow, B.J., and Sala, A. (2003). Essential Requirement of Apolipoprotein J (Clusterin) Signaling for IκB Expression and Regulation of NF-κB Activity *. J. Biol. Chem. *278*, 38214–38219. https://doi.org/10.1074/jbc.C300252200.
30. Devauchelle, V., Essabbani, A., De Pinieux, G., Germain, S., Tourneur, L., Mistou, S., Margottin-Goguet, F., Anract, P., Migaud, H., Le Nen, D., et al. (2006). Characterization and functional consequences of underexpression of clusterin in rheumatoid arthritis. J. Immunol. *177*, 6471–6479. https://doi.org/10.4049/jimmunol.177.9.6471.
31. Essabbani, A., Margottin-Goguet, F., and Chiocchia, G. (2010). Identification of Clusterin Domain Involved in NF-κB Pathway Regulation 2. J. Biol. Chem. *285*, 4273–4277. https://doi.org/10.1074/jbc.C109.057133.
32. Takase, O., Minto, A.W.M., Puri, T.S., Cunningham, P.N., Jacob, A., Hayashi, M., and Quigg, R.J. (2008). Inhibition of NF-kappaB-dependent Bcl-xL expression by clusterin promotes albumin-induced tubular cell apoptosis. Kidney Int. *73*, 567–577. https://doi.org/10.1038/sj.ki.5002563.
33. Venegas, C., and Heneka, M.T. (2019). Inflammasome-mediated innate immunity in Alzheimer's disease. FASEB J. *33*, 13075–13084. https://doi.org/10.1096/fj.201900439.
34. Itagaki, S., McGeer, P.L., Akiyama, H., Zhu, S., and Selkoe, D. (1989). Relationship of microglia and astrocytes to amyloid deposits of Alzheimer disease. J. Neuroimmunol. *24*, 173–182. https://doi.org/10.1016/0165-5728(89)90115-x.
35. Paolicelli, R.C., Sierra, A., Stevens, B., Tremblay, M.-E., Aguzzi, A., Ajami, B., Amit, I., Audinat, E., Bechmann, I., Bennett, M., et al. (2022). Microglia states and nomenclature: A field at its crossroads. Neuron *110*, 3458–3483. https://doi.org/10.1016/j.neuron.2022.10.020.
36. Liddelow, S.A., Guttenplan, K.A., Clarke, L.E., Bennett, F.C., Bohlen, C.J., Schirmer, L., Bennett, M.L., Münch, A.E., Chung, W.-S., Peterson, T.C., et al. (2017). Neurotoxic reactive astrocytes are induced by activated microglia. Nature *541*, 481–487. https://doi.org/10.1038/nature21029.
37. Stevens, B., Allen, N.J., Vazquez, L.E., Howell, G.R., Christopherson, K.S., Nouri, N., Micheva, K.D., Mehalow, A.K., Huberman, A.D., Stafford, B., et al. (2007). The classical complement cascade mediates CNS synapse elimination. Cell *131*, 1164–1178. https://doi.org/10.1016/j.cell.2007.10.036.
38. Shinjyo, N., Ståhlberg, A., Dragunow, M., Pekny, M., and Pekna, M. (2009). Complement-derived anaphylatoxin C3a regulates in vitro

differentiation and migration of neural progenitor cells. Stem Cells *27*, 2824–2832. https://doi.org/10.1002/stem.225.

39. Benoit, M.E., and Tenner, A.J. (2011). Complement protein C1q-mediated neuroprotection is correlated with regulation of neuronal gene and microRNA expression. J. Neurosci. *31*, 3459–3469. https://doi.org/10.1523/JNEUROSCI.3932-10.2011.
40. Bradt, B.M., Kolb, W.P., and Cooper, N.R. (1998). Complement-dependent proinflammatory properties of the Alzheimer's disease beta-peptide. J. Exp. Med. *188*, 431–438. https://doi.org/10.1084/jem.188.3.431.
41. Fan, R., and Tenner, A.J. (2004). Complement C1q expression induced by Abeta in rat hippocampal organotypic slice cultures. Exp. Neurol. *185*, 241–253. https://doi.org/10.1016/j.expneurol.2003.09.023.
42. Loeffler, D.A., Camp, D.M., and Bennett, D.A. (2008). Plaque complement activation and cognitive loss in Alzheimer's disease. J. Neuroinflammation *5*, 9. https://doi.org/10.1186/1742-2094-5-9.
43. Batista, A.F., Khan, K.A., Papavergi, M.-T., and Lemere, C.A. (2024). The Importance of Complement-Mediated Immune Signaling in Alzheimer's Disease Pathogenesis. Int. J. Mol. Sci. *25*, 817. https://doi.org/10.3390/ijms25020817.
44. Nilselid, A.M., Davidsson, P., Nägga, K., Andreasen, N., Fredman, P., and Blennow, K. (2006). Clusterin in cerebrospinal fluid: analysis of carbohydrates and quantification of native and glycosylated forms. Neurochem. Int. *48*, 718–728. https://doi.org/10.1016/j.neuint.2005.12.005.
45. Bennett, D.A., Schneider, J.A., Buchman, A.S., Barnes, L.L., Boyle, P.A., and Wilson, R.S. (2012). Overview and findings from the rush Memory and Aging Project. Curr. Alzheimer Res. *9*, 646–663. https://doi.org/10.2174/156720512801322663.
46. Bennett, D.A., Schneider, J.A., Arvanitakis, Z., and Wilson, R.S. (2012). Overview and findings from the religious orders study. Curr. Alzheimer Res. *9*, 628–645. https://doi.org/10.2174/156720512801322573.
47. Bennett, D.A., Buchman, A.S., Boyle, P.A., Barnes, L.L., Wilson, R.S., and Schneider, J.A. (2018). Religious Orders Study and Rush Memory and Aging Project. J. Alzheimers Dis. *64*, S161–S189. https://doi.org/10.3233/JAD-179939.
48. De Jager, P.L., Ma, Y., McCabe, C., Xu, J., Vardarajan, B.N., Felsky, D., Klein, H.-U., White, C.C., Peters, M.A., Lodgson, B., et al. (2018). A multi-omic atlas of the human frontal cortex for aging and Alzheimer's disease research. Sci. Data *5*, 180142. https://doi.org/10.1038/sdata.2018.142.
49. Schneider, J.A., Arvanitakis, Z., Leurgans, S.E., and Bennett, D.A. (2009). The neuropathology of probable Alzheimer disease and mild cognitive impairment. Ann. Neurol. *66*, 200–208. https://doi.org/10.1002/ana.21706.
50. Vialle, R.A., de Paiva Lopes, K., Li, Y., Ng, B., Schneider, J.A., Buchman, A.S., Wang, Y., Farfel, J.M., Barnes, L.L., Wingo, A.P., et al. (2024). Structural variants linked to Alzheimer's Disease and other common age-related clinical and neuropathologic traits. Preprint at medRxiv. https://doi.org/10.1101/2024.08.12.24311887.
51. Green, G.S., Fujita, M., Yang, H.-S., Taga, M., Cain, A., McCabe, C., Comandante-Lou, N., White, C.C., Schmidtner, A.K., Zeng, L., et al. (2024). Cellular communities reveal trajectories of brain ageing and Alzheimer's disease. Nature *633*, 634–645. https://doi.org/10.1038/s41586-024-07871-6.
52. Bennett, D.A., Schneider, J.A., Wilson, R.S., Bienias, J.L., and Arnold, S.E. (2004). Neurofibrillary tangles mediate the association of amyloid load with clinical Alzheimer disease and level of cognitive function. Arch. Neurol. *61*, 378–384. https://doi.org/10.1001/archneur.61.3.378.
53. Bennett, D.A., Schneider, J.A., Wilson, R.S., Bienias, J.L., and Arnold, S.E. (2005). Education modifies the association of amyloid but not tangles with cognitive function. Neurology *65*, 953–955. https://doi.org/10.1212/01.wnl.0000176286.17192.69.
54. Barnes, L.L., Schneider, J.A., Boyle, P.A., Bienias, J.L., and Bennett, D.A. (2006). Memory complaints are related to Alzheimer disease pathology in older persons. Neurology *67*, 1581–1585. https://doi.org/10.1212/01.wnl.0000242734.16663.09.
55. Canals, I., Ginisty, A., Quist, E., Timmerman, R., Fritze, J., Miskinyte, G., Monni, E., Hansen, M.G., Hidalgo, I., Bryder, D., et al. (2019). Author Correction: Rapid and efficient induction of functional astrocytes from human pluripotent stem cells. Nat. Methods *16*, 134. https://doi.org/10.1038/s41592-018-0264-z.
56. Lee, H., Pearse, R.V., 2nd, Lish, A.M., Pan, C., Augur, Z.M., Terzioglu, G., Gaur, P., Liao, M., Fujita, M., Tio, E.S., et al. (2025). Contributions of genetic variation in astrocytes to cell and molecular mechanisms of risk and resilience to late-onset Alzheimer's disease. Glia. https://doi.org/10.1002/glia.24677.
57. Subramanian, A., Tamayo, P., Mootha, V.K., Mukherjee, S., Ebert, B.L., Gillette, M.A., Paulovich, A., Pomeroy, S.L., Golub, T.R., Lander, E.S., et al. (2005). Gene set enrichment analysis: a knowledge-based approach for interpreting genome-wide expression profiles. Proc. Natl. Acad. Sci. USA *102*, 15545–15550. https://doi.org/10.1073/pnas.0506580102.
58. Liu, T., Zhang, L., Joo, D., and Sun, S.-C. (2017). NF-κB signaling in inflammation. Signal Transduct. Target. Ther. *2*, 17023. https://doi.org/10.1038/sigtrans.2017.23.
59. Hannink, M., and Temin, H.M. (1990). Structure and autoregulation of the c-rel promoter. Oncogene *5*, 1843–1850.
60. Lian, H., Yang, L., Cole, A., Sun, L., Chiang, A.C.-A., Fowler, S.W., Shim, D.J., Rodriguez-Rivera, J., Taglialatela, G., Jankowsky, J.L., et al. (2015). NFκB-activated astroglial release of complement C3 compromises neuronal morphology and function associated with Alzheimer's disease. Neuron *85*, 101–115. https://doi.org/10.1016/j.neuron.2014.11.018.
61. Lian, H., Litvinchuk, A., Chiang, A.C.-A., Aithmitti, N., Jankowsky, J.L., and Zheng, H. (2016). Astrocyte-Microglia Cross Talk through Complement Activation Modulates Amyloid Pathology in Mouse Models of Alzheimer's Disease. J. Neurosci. *36*, 577–589. https://doi.org/10.1523/JNEUROSCI.2117-15.2016.
62. Bell, R.D., Sagare, A.P., Friedman, A.E., Bedi, G.S., Holtzman, D.M., Deane, R., and Zlokovic, B.V. (2007). Transport Pathways for Clearance of Human Alzheimer's Amyloid β-Peptide and Apolipoproteins E and J in the Mouse Central Nervous System. J. Cereb. Blood Flow Metab. *27*, 909–918. https://doi.org/10.1038/sj.jcbfm.9600419.
63. Oda, T., Wals, P., Osterburg, H.H., Johnson, S.A., Pasinetti, G.M., Morgan, T.E., Rozovsky, I., Stine, W.B., Snyder, S.W., and Holzman, T.F. (1995). Clusterin (apoJ) Alters the Aggregation of Amyloid β-Peptide (Aβ1-42) and Forms Slowly Sedimenting Aβ Complexes That Cause Oxidative Stress. Exp. Neurol. *136*, 22–31. https://doi.org/10.1006/exnr.1995.1080.
64. Zlokovic, B.V., Martel, C.L., Matsubara, E., McComb, J.G., Zheng, G., McCluskey, R.T., Frangione, B., and Ghiso, J. (1996). Glycoprotein 330/megalin: probable role in receptor-mediated transport of apolipoprotein J alone and in a complex with Alzheimer disease amyloid beta at the blood-brain and blood-cerebrospinal fluid barriers. Proc. Natl. Acad. Sci. USA *93*, 4229–4234. https://doi.org/10.1073/pnas.93.9.4229.
65. Matsubara, E., Soto, C., Governale, S., Frangione, B., and Ghiso, J. (1996). Apolipoprotein J and Alzheimer's amyloid beta solubility. Biochem. J. *316*, 671–679. https://doi.org/10.1042/bj3160671.
66. Calero, M., Rostagno, A., Matsubara, E., Zlokovic, B., Frangione, B., and Ghiso, J. (2000). Apolipoprotein J (clusterin) and Alzheimer's disease. Microsc. Res. Tech. *50*, 305–315. https://doi.org/10.1002/1097-0029(20000815)50:4<305::AID-JEMT10>3.0.CO;2-L.
67. Wojtas, A.M., Carlomagno, Y., Sens, J.P., Kang, S.S., Jensen, T.D., Kurti, A., Baker, K.E., Berry, T.J., Phillips, V.R., Castanedes, M.C., et al. (2020). Clusterin ameliorates tau pathology in vivo by inhibiting fibril formation. Acta Neuropathol. Commun. *8*, 210. https://doi.org/10.1186/s40478-020-01079-1.
68. Yuste-Checa, P., Trinkaus, V.A., Riera-Tur, I., Imamoglu, R., Schaller, T.F., Wang, H., Dudanova, I., Hipp, M.S., Bracher, A., and Hartl, F.U. (2021). The extracellular chaperone Clusterin enhances Tau aggregate

seeding in a cellular model. Nat. Commun. *12*, 4863. https://doi.org/10.1038/s41467-021-25060-1.

69. Sadick, J.S., O'Dea, M.R., Hasel, P., Dykstra, T., Faustin, A., and Liddelow, S.A. (2022). Astrocytes and oligodendrocytes undergo subtype-specific transcriptional changes in Alzheimer's disease. Neuron *110*, 1788–1805.e10. https://doi.org/10.1016/j.neuron.2022.03.008.

70. Lo, C.H., Skarica, M., Mansoor, M., Bhandarkar, S., Toro, S., and Pitt, D. (2021). Astrocyte Heterogeneity in Multiple Sclerosis: Current Understanding and Technical Challenges. Front. Cell. Neurosci. *15*, 726479. https://doi.org/10.3389/fncel.2021.726479.

71. Keren-Shaul, H., Spinrad, A., Weiner, A., Matcovitch-Natan, O., Dvir-Szternfeld, R., Ulland, T.K., David, E., Baruch, K., Lara-Astaiso, D., Toth, B., et al. (2017). A Unique Microglia Type Associated with Restricting Development of Alzheimer's Disease. Cell *169*, 1276–1290.e17. https://doi.org/10.1016/j.cell.2017.05.018.

72. Yeh, F.L., Wang, Y., Tom, I., Gonzalez, L.C., and Sheng, M. (2016). TREM2 Binds to Apolipoproteins, Including APOE and CLU/APOJ, and Thereby Facilitates Uptake of Amyloid-Beta by Microglia. Neuron *91*, 328–340. https://doi.org/10.1016/j.neuron.2016.06.015.

73. Zhong, L., Sheng, X., Wang, W., Li, Y., Zhuo, R., Wang, K., Zhang, L., Hu, D.-D., Hong, Y., Chen, L., et al. (2023). TREM2 receptor protects against complement-mediated synaptic loss by binding to complement C1q during neurodegeneration. Immunity *56*, 1794–1808.e8. https://doi.org/10.1016/j.immuni.2023.06.016.

74. Haass, C. (2021). Loss of TREM2 facilitates tau accumulation, spreading, and brain atrophy, but only in the presence of amyloid pathology. Neuron *109*, 1243–1245. https://doi.org/10.1016/j.neuron.2021.03.029.

75. Jain, N., Lewis, C.A., Ulrich, J.D., and Holtzman, D.M. (2023). Chronic TREM2 activation exacerbates Aβ-associated tau seeding and spreading. J. Exp. Med. *220*, e20220654. https://doi.org/10.1084/jem.20220654.

76. Taylor, X., Cisternas, P., You, Y., You, Y., Xiang, S., Marambio, Y., Zhang, J., Vidal, R., and Lasagna-Reeves, C.A. (2020). A1 reactive astrocytes and a loss of TREM2 are associated with an early stage of pathology in a mouse model of cerebral amyloid angiopathy. J. Neuroinflammation *17*, 223. https://doi.org/10.1186/s12974-020-01900-7.

77. Dräger, N.M., Sattler, S.M., Huang, C.T.-L., Teter, O.M., Leng, K., Hashemi, S.H., Hong, J., Aviles, G., Clelland, C.D., Zhan, L., et al. (2022). A CRISPRi/a platform in human iPSC-derived microglia uncovers regulators of disease states. Nat. Neurosci. *25*, 1149–1162. https://doi.org/10.1038/s41593-022-01131-4.

78. Dolan, M.-J., Therrien, M., Jereb, S., Kamath, T., Gazestani, V., Atkeson, T., Marsh, S.E., Goeva, A., Lojek, N.M., Murphy, S., et al. (2023). Exposure of iPSC-derived human microglia to brain substrates enables the generation and manipulation of diverse transcriptional states in vitro. Nat. Immunol. *24*, 1382–1390. https://doi.org/10.1038/s41590-023-01558-2.

79. Thomas, E.V., Han, C., Kim, W.J., Asress, S., Li, Y., Taylor, J.A., Gearing, M., Fournier, C.N., McEachin, Z.T., Seyfried, N.T., et al. (2025). ALS plasma biomarkers reveal neurofilament and pTau correlate with disease onset and progression. Ann. Clin. Transl. Neurol. https://doi.org/10.1002/acn3.70001.

80. Lagomarsino, V.N., Pearse, R.V., 2nd, Liu, L., Hsieh, Y.-C., Fernandez, M.A., Vinton, E.A., Paull, D., Felsky, D., Tasaki, S., Gaiteri, C., et al. (2021). Stem cell-derived neurons reflect features of protein networks, neuropathology, and cognitive outcome of their aged human donors. Neuron *109*, 3402–3420.e9. https://doi.org/10.1016/j.neuron.2021.08.003.

81. Thambisetty, M., An, Y., Kinsey, A., Koka, D., Saleem, M., Güntert, A., Kraut, M., Ferrucci, L., Davatzikos, C., Lovestone, S., et al. (2012). Plasma clusterin concentration is associated with longitudinal brain atrophy in mild cognitive impairment. Neuroimage *59*, 212–217. https://doi.org/10.1016/j.neuroimage.2011.07.056.

82. Haight, T., Bryan, R.N., Meirelles, O., Tracy, R., Fornage, M., Richard, M., Nasrallah, I., Yaffe, K., Jacobs, D.R., Jr., Lewis, C., et al. (2018). Associations of plasma clusterin and Alzheimer's disease-related MRI markers in adults at mid-life: The CARDIA Brain MRI sub-study. PLoS One *13*, e0190478. https://doi.org/10.1371/journal.pone.0190478.

83. Desikan, R.S., Thompson, W.K., Holland, D., Hess, C.P., Brewer, J.B., Zetterberg, H., Blennow, K., Andreassen, O.A., McEvoy, L.K., Hyman, B.T., et al. (2014). The Role of Clusterin in Amyloid-β–Associated Neurodegeneration. JAMA Neurol. *71*, 180–187. https://doi.org/10.1001/jamaneurol.2013.4560.

84. DeMattos, R.B., O'Dell, M.A., Parsadanian, M., Taylor, J.W., Harmony, J.A.K., Bales, K.R., Paul, S.M., Aronow, B.J., and Holtzman, D.M. (2002). Clusterin promotes amyloid plaque formation and is critical for neuritic toxicity in a mouse model of Alzheimer's disease. Proc. Natl. Acad. Sci. USA *99*, 10843–10848. https://doi.org/10.1073/pnas.162228299.

85. Wojtas, A.M., Sens, J.P., Kang, S.S., Baker, K.E., Berry, T.J., Kurti, A., Daughrity, L., Jansen-West, K.R., Dickson, D.W., Petrucelli, L., et al. (2020). Astrocyte-derived clusterin suppresses amyloid formation in vivo. Mol. Neurodegener. *15*, 71. https://doi.org/10.1186/s13024-020-00416-1.

86. Giannakopoulos, P., Herrmann, F.R., Bussière, T., Bouras, C., Kövari, E., Perl, D.P., Morrison, J.H., Gold, G., and Hof, P.R. (2003). Tangle and neuron numbers, but not amyloid load, predict cognitive status in Alzheimer's disease. Neurology *60*, 1495–1500. https://doi.org/10.1212/01.wnl.0000063311.58879.01.

87. Brier, M.R., Gordon, B., Friedrichsen, K., McCarthy, J., Stern, A., Christensen, J., Owen, C., Aldea, P., Su, Y., Hassenstab, J., et al. (2016). Tau and Aβ imaging, CSF measures, and cognition in Alzheimer's disease. Sci. Transl. Med. *8*, 338ra66. https://doi.org/10.1126/scitranslmed.aaf2362.

88. Scott-Hewitt, N., Mahoney, M., Huang, Y., Korte, N., Yvanka de Soysa, T., Wilton, D.K., Knorr, E., Mastro, K., Chang, A., Zhang, A., et al. (2024). Microglial-derived C1q integrates into neuronal ribonucleoprotein complexes and impacts protein homeostasis in the aging brain. Cell *187*, 4193–4212.e24. https://doi.org/10.1016/j.cell.2024.05.058.

89. Maziuk, B.F., Apicco, D.J., Cruz, A.L., Jiang, L., Ash, P.E.A., da Rocha, E.L., Zhang, C., Yu, W.H., Leszyk, J., Abisambra, J.F., et al. (2018). RNA binding proteins co-localize with small tau inclusions in tauopathy. Acta Neuropathol. Commun. *6*, 71. https://doi.org/10.1186/s40478-018-0574-5.

90. Vanderweyde, T., Apicco, D.J., Youmans-Kidder, K., Ash, P.E.A., Cook, C., Lummertz da Rocha, E., Jansen-West, K., Frame, A.A., Citro, A., Leszyk, J.D., et al. (2016). Interaction of tau with the RNA-Binding Protein TIA1 Regulates tau Pathophysiology and Toxicity. Cell Rep. *15*, 1455–1466. https://doi.org/10.1016/j.celrep.2016.04.045.

91. Tschopp, J., and French, L.E. (1994). Clusterin: modulation of complement function. Clin. Exp. Immunol. *97*, 11–14. https://doi.org/10.1111/j.1365-2249.1994.tb06256.x.

92. Tschopp, J., Chonn, A., Hertig, S., and French, L.E. (1993). Clusterin, the human apolipoprotein and complement inhibitor, binds to complement C7, C8 beta, and the b domain of C9. J. Immunol. *151*, 2159–2165. https://doi.org/10.4049/jimmunol.151.4.2159.

93. Murphy, B.F., Saunders, J.R., O'Bryan, M.K., Kirszbaum, L., Walker, I.D., and d'Apice, A.J.F. (1989). SP-40,40 is an inhibitor of C5b-6-initiated haemolysis. Int. Immunol. *1*, 551–554. https://doi.org/10.1093/intimm/1.5.551.

94. Choi, N.H., Nakano, Y., Tobe, T., Mazda, T., and Tomita, M. (1990). Incorporation of SP-40,40 into the soluble membrane attack complex (SMAC, SC5b-9) of complement. Int. Immunol. *2*, 413–417. https://doi.org/10.1093/intimm/2.5.413.

95. O'Bryan, M.K., Baker, H.W., Saunders, J.R., Kirszbaum, L., Walker, I.D., Hudson, P., Liu, D.Y., Glew, M.D., d'Apice, A.J., and Murphy, B.F. (1990). Human seminal clusterin (SP-40,40). Isolation and characterization. J. Clin. Invest. *85*, 1477–1486. https://doi.org/10.1172/JCI114594.

96. De Miguel, Z., Khoury, N., Betley, M.J., Lehallier, B., Willoughby, D., Olsson, N., Yang, A.C., Hahn, O., Lu, N., Vest, R.T., et al. (2021). Exercise plasma boosts memory and dampens brain inflammation via clusterin. Nature *600*, 494–499. https://doi.org/10.1038/s41586-021-04183-x.

97. Yin, C., Ackermann, S., Ma, Z., Mohanta, S.K., Zhang, C., Li, Y., Nietzsche, S., Westermann, M., Peng, L., Hu, D., et al. (2019). ApoE attenuates unresolvable inflammation by complex formation with activated C1q. Nat. Med. *25*, 496–506. https://doi.org/10.1038/s41591-018-0336-8.

98. Qu, W., and Li, L. (2020). Loss of TREM2 Confers Resilience to Synaptic and Cognitive Impairment in Aged Mice. J. Neurosci. *40*, 9552–9563. https://doi.org/10.1523/JNEUROSCI.2193-20.2020.

99. Filipello, F., Morini, R., Corradini, I., Zerbi, V., Canzi, A., Michalski, B., Erreni, M., Markicevic, M., Starvaggi-Cucuzza, C., Otero, K., et al. (2018). The Microglial Innate Immune Receptor TREM2 Is Required for Synapse Elimination and Normal Brain Connectivity. Immunity *48*, 979–991.e8. https://doi.org/10.1016/j.immuni.2018.04.016.

100. Zhao, J., Fu, Y., Yamazaki, Y., Ren, Y., Davis, M.D., Liu, C.-C., Lu, W., Wang, X., Chen, K., Cherukuri, Y., et al. (2021). Author Correction: APOE4 exacerbates synapse loss and neurodegeneration in Alzheimer's disease patient iPSC-derived cerebral organoids. Nat. Commun. *12*, 2707. https://doi.org/10.1038/s41467-021-23081-4.

101. Trougakos, I.P., Petropoulou, C., Franceschi, C., and Gonos, E.S. (2006). Reduced expression levels of the senescence biomarker clusterin/apolipoprotein j in lymphocytes from healthy centenarians. Ann. N. Y. Acad. Sci. *1067*, 294–300. https://doi.org/10.1196/annals.1354.039.

102. He, J., Dijkstra, K.L., Bakker, K., Bus, P., Bruijn, J.A., Scharpfenecker, M., and Baelde, H.J. (2020). Glomerular clusterin expression is increased in diabetic nephropathy and protects against oxidative stress-induced apoptosis in podocytes. Sci. Rep. *10*, 14888. https://doi.org/10.1038/s41598-020-71629-z.

103. Zhang, Y., Pak, C., Han, Y., Ahlenius, H., Zhang, Z., Chanda, S., Marro, S., Patzke, C., Acuna, C., Covy, J., et al. (2013). Rapid single-step induction of functional neurons from human pluripotent stem cells. Neuron *78*, 785–798. https://doi.org/10.1016/j.neuron.2013.05.029.

104. Seifar, F., Fox, E.J., Shantaraman, A., Liu, Y., Dammer, E.B., Modeste, E., Duong, D.M., Yin, L., Trautwig, A.N., Guo, Q., et al. (2024). Large-scale deep proteomic analysis in Alzheimer's disease brain regions across race and ethnicity. Preprint at bioRxiv. https://doi.org/10.1101/2024.04.22.590547.

105. Paquet, D., Kwart, D., Chen, A., Sproul, A., Jacob, S., Teo, S., Olsen, K.M., Gregg, A., Noggle, S., and Tessier-Lavigne, M. (2016). Efficient introduction of specific homozygous and heterozygous mutations using CRISPR/Cas9. Nature *533*, 125–129. https://doi.org/10.1038/nature17664.

106. R Core Team (2021). A language and environment for statistical computing.

107. Zheng, G.X.Y., Terry, J.M., Belgrader, P., Ryvkin, P., Bent, Z.W., Wilson, R., Ziraldo, S.B., Wheeler, T.D., McDermott, G.P., Zhu, J., et al. (2017). Massively parallel digital transcriptional profiling of single cells. Nat. Commun. *8*, 14049. https://doi.org/10.1038/ncomms14049.

108. Satija, R., Farrell, J.A., Gennert, D., Schier, A.F., and Regev, A. (2015). Spatial reconstruction of single-cell gene expression data. Nat. Biotechnol. *33*, 495–502. https://doi.org/10.1038/nbt.3192.

109. Schindelin, J., Arganda-Carreras, I., Frise, E., Kaynig, V., Longair, M., Pietzsch, T., Preibisch, S., Rueden, C., Saalfeld, S., Schmid, B., et al. (2012). Fiji: an open-source platform for biological-image analysis. Nat. Methods *9*, 676–682. https://doi.org/10.1038/nmeth.2019.

110. Rodriguez, A., Ehlenberger, D.B., Hof, P.R., and Wearne, S.L. (2006). Rayburst sampling, an algorithm for automated three-dimensional shape analysis from laser scanning microscopy images. Nat. Protoc. *1*, 2152–2161. https://doi.org/10.1038/nprot.2006.313.

111. Wilson, R.S., Arnold, S.E., Schneider, J.A., Tang, Y., and Bennett, D.A. (2007). The relationship between cerebral Alzheimer's disease pathology and odour identification in old age. J. Neurol. Neurosurg. Psychiatry *78*, 30–35. https://doi.org/10.1136/jnnp.2006.099721.

112. Bennett, D.A., and Barnes, L.L. (2011). Datasets for special series on cognitive reserve. J. Int. Neuropsychol. Soc. *17*, 587–592. https://doi.org/10.1017/S1355617711000622.

113. Stern, A.M., Yang, Y., Jin, S., Yamashita, K., Meunier, A.L., Liu, W., Cai, Y., Ericsson, M., Liu, L., Goedert, M., et al. (2023). Abundant Aβ fibrils in ultracentrifugal supernatants of aqueous extracts from Alzheimer's disease brains. Neuron *111*, 2012–2020.e4. https://doi.org/10.1016/j.neuron.2023.04.007.

114. Hong, W., Wang, Z., Liu, W., O'Malley, T.T., Jin, M., Willem, M., Haass, C., Frosch, M.P., and Walsh, D.M. (2018). Diffusible, highly bioactive oligomers represent a critical minority of soluble Aβ in Alzheimer's disease brain. Acta Neuropathol. *136*, 19–40. https://doi.org/10.1007/s00401-018-1846-7.

115. Kwart, D., Gregg, A., Scheckel, C., Murphy, E.A., Paquet, D., Duffield, M., Fak, J., Olsen, O., Darnell, R.B., and Tessier-Lavigne, M. (2019). A Large Panel of Isogenic APP and PSEN1 Mutant Human iPSC Neurons Reveals Shared Endosomal Abnormalities Mediated by APP β-CTFs, Not Aβ. Neuron *104*, 256–270.e5. https://doi.org/10.1016/j.neuron.2019.07.010.

116. Lee, H., Aylward, A.J., Pearse, R.V., 2nd, Lish, A.M., Hsieh, Y.-C., Augur, Z.M., Benoit, C.R., Chou, V., Knupp, A., Pan, C., et al. (2023). Cell-type-specific regulation of APOE and CLU levels in human neurons by the Alzheimer's disease risk gene SORL1. Cell Rep. *42*, 112994. https://doi.org/10.1016/j.celrep.2023.112994.

117. Abud, E.M., Ramirez, R.N., Martinez, E.S., Healy, L.M., Nguyen, C.H.H., Newman, S.A., Yeromin, A.V., Scarfone, V.M., Marsh, S.E., Fimbres, C., et al. (2017). iPSC-Derived Human Microglia-like Cells to Study Neurological Diseases. Neuron *94*, 278–293.e9. https://doi.org/10.1016/j.neuron.2017.03.042.

118. McQuade, A., Coburn, M., Tu, C.H., Hasselmann, J., Davtyan, H., and Blurton-Jones, M. (2018). Development and validation of a simplified method to generate human microglia from pluripotent stem cells. Mol. Neurodegener. *13*, 67. https://doi.org/10.1186/s13024-018-0297-x.

119. Chou, V., Pearse, R.V., 2nd, Aylward, A.J., Ashour, N., Taga, M., Terzioglu, G., Fujita, M., Fancher, S.B., Sigalov, A., Benoit, C.R., et al. (2023). INPP5D regulates inflammasome activation in human microglia. Nat. Commun. *14*, 7552. https://doi.org/10.1038/s41467-023-42819-w.

120. Muratore, C.R., Zhou, C., Liao, M., Fernandez, M.A., Taylor, W.M., Lagomarsino, V.N., Pearse, R.V., 2nd, Rice, H.C., Negri, J.M., He, A., et al. (2017). Cell-type Dependent Alzheimer's Disease Phenotypes: Probing the Biology of Selective Neuronal Vulnerability. Stem Cell Rep. *9*, 1868–1884. https://doi.org/10.1016/j.stemcr.2017.10.015.

121. Waelchli, R., Bollbuck, B., Bruns, C., Buhl, T., Eder, J., Feifel, R., Hersperger, R., Janser, P., Revesz, L., Zerwes, H.-G., et al. (2006). Design and preparation of 2-benzamido-pyrimidines as inhibitors of IKK. Bioorg. Med. Chem. Lett. *16*, 108–112. https://doi.org/10.1016/j.bmcl.2005.09.035.

122. Ping, L., Duong, D.M., Yin, L., Gearing, M., Lah, J.J., Levey, A.I., and Seyfried, N.T. (2018). Global quantitative analysis of the human brain proteome in Alzheimer's and Parkinson's Disease. Sci. Data *5*, 180036. https://doi.org/10.1038/sdata.2018.36.

123. Leek, J.T., Johnson, W.E., Parker, H.S., Jaffe, A.E., and Storey, J.D. (2012). The sva package for removing batch effects and other unwanted variation in high-throughput experiments. Bioinformatics *28*, 882–883. https://doi.org/10.1093/bioinformatics/bts034.

124. Higginbotham, L., Ping, L., Dammer, E.B., Duong, D.M., Zhou, M., Gearing, M., Hurst, C., Glass, J.D., Factor, S.A., Johnson, E.C.B., et al. (2020). Integrated proteomics reveals brain-based cerebrospinal fluid biomarkers in asymptomatic and symptomatic Alzheimer's disease. Sci. Adv. *6*, eaaz9360. https://doi.org/10.1126/sciadv.aaz9360.

125. Ping, L., Kundinger, S.R., Duong, D.M., Yin, L., Gearing, M., Lah, J.J., Levey, A.I., and Seyfried, N.T. (2020). Global quantitative analysis of the human brain proteome and phosphoproteome in Alzheimer's disease. Sci. Data *7*, 315. https://doi.org/10.1038/s41597-020-00650-8.

126. Zhang, X., Smits, A.H., van Tilburg, G.B., Ovaa, H., Huber, W., and Vermeulen, M. (2018). Proteome-wide identification of ubiquitin interactions using UbIA-MS. Nat. Protoc. *13*, 530–550. https://doi.org/10.1038/nprot.2017.147.

127. Korotkevich, G., Sukhov, V., Budin, N., Shpak, B., Artyomov, M.N., and Sergushichev, A. (2016). Fast gene set enrichment analysis. Preprint at bioRxiv. https://doi.org/10.1101/060012.

128. Patro, R., Duggal, G., Love, M.I., Irizarry, R.A., and Kingsford, C. (2017). Salmon provides fast and bias-aware quantification of transcript expression. Nat. Methods *14*, 417–419. https://doi.org/10.1038/nmeth.4197.

129. Love, M.I., Huber, W., and Anders, S. (2014). Moderated estimation of fold change and dispersion for RNA-seq data with DESeq2. Genome Biol. *15*, 550. https://doi.org/10.1186/s13059-014-0550-8.

130. Cheng, C., Trzcinski, O., and Doering, L.C. (2014). Fluorescent labeling of dendritic spines in cell cultures with the carbocyanine dye "DiI.". Front. Neuroanat. *8*, 30. https://doi.org/10.3389/fnana.2014.00030.

131. Stirling, D.R., Swain-Bowden, M.J., Lucas, A.M., Carpenter, A.E., Cimini, B.A., and Goodman, A. (2021). CellProfiler 4: improvements in speed, utility and usability. BMC Bioinformatics *22*, 433. https://doi.org/10.1186/s12859-021-04344-9.

Please cite this article in press as: Lish et al., CLU alleviates Alzheimer's disease-relevant processes by modulating astrocyte reactivity and microglia-dependent synaptic density, Neuron (2025), https://doi.org/10.1016/j.neuron.2025.03.034

STAR★METHODS

KEY RESOURCES TABLE

REAGENT or RESOURCE	SOURCE	IDENTIFIER
Antibodies		
Mouse anti-phospho-tau (Ser202, Thr205)	Thermo Fisher Scientific	Cat# MN1020; RRID:AB_223647
Mouse anti-GAPDH	Proteintech	Cat# 60004-1-Ig; RRID:AB_2107436
Chicken anti-GFAP	Abcam	Cat# ab4674; RRID:AB_304558
Goat anti-AIF1	Abcam	Cat# ab5076; RRID:AB_2224402
Rabbit anti-clusterin	Abcam	Cat# ab92548; RRID:AB_10585132
Rabbit anti-ICAM-1	Cell Signaling Technologies	Cat# 4915; RRID:AB_2280018
Mouse anti-IkBa	Cell Signaling Technologies	Cat# 4814S; RRID:AB_390781
Rabbit anti-S100B	Abcam	Cat# ab52642; RRID:AB_882426
Chicken anti-TUJ1	Novus	Cat# nb100-1612; RRID: AB_10000548
Rabbit anti-TAU	Cell Signaling Technologies	Cat# 46687S; RRID:AB_2783844
Rabbit anti-TREM2	Abcam	Cat# ab209814; RID:AB_3095849
Mouse anti-vimentin	Millipore	Cat# CBL202; RRID:AB_93387
Mouse anti-CD44	Abcam	Cat# ab254530; RRID: AB_2885131
Mouse anti-VGLUT2	Abcam	Cat# ab79157; RRID:AB_1603114
Rabbit anti-HOMER1	Synaptic Systems	Cat# 160003; RRID:AB_887730
Rabbit anti-NeuN	Abcam	Cat # ab177487; RRID: AB_2532109
Rabbit pTAU-217	GeneTex	Cat # GTX135775; RRID: AB_2909879
Rabbit pTAU-214	Cell Signaling	Cat # 77348; RRID: AB_2799895
Bacterial and virus strains		
pTet-O-NGN2-puro	Zhang et al.[103]	Addgene plasmid #52047
FUdeltaGW-rtTA	Zhang et al.[103]	Addgene plasmid #19780
Tet-O-SOX9-puro	Canals et al.[55]	Addgene plasmid #117269
Tet-O-NFIB-hygro	Canals et al.[55]	Addgene plasmid #117271
pGL4.32[*luc2P*/NF-κB-RE/Hygro]	Promega	#E849A
pRL-CMV	Promega	#E2261
pRP[Exp]-CMV>eGFP-CAG>hCLU[NM_001831.4]	VectorBuilder	N/A
pmax-CMV>eGFP	Lonza	Plasma #177825
Biological samples		
Postmortem brain tissues (Table S1)	Religious Orders Study and Rush Memory and Aging Project	N/A
Plasma (Table S7)	Religious Orders Study and Rush Memory and Aging Project	N/A
Chemicals, peptides, and recombinant proteins		
TNF	Fisher Scientific	Cat #210TA020
IKK Inhibitor VII	Millipore	Cat #401486
IL1B	Fisher Scientific	Cat# 201LB005
C1q	MyBioSource	Cat# MBS147305
1,1′-dioctadecyl-3,3,3′,3′-tetramethylindocarbocyanine perchlorate	Invitrogen	Cat# D282
Critical commercial assays		
R-PLEX Human ApoE Assay	Meso Scale Discovery	Cat. #K1512IR-2
R-PLEX Human C3 Assay	Meso Scale Discovery	Cat. #F21XY-3

(*Continued on next page*)

Continued

REAGENT or RESOURCE	SOURCE	IDENTIFIER
U-PLEX Human CLU Assay	Meso Scale Discovery	Cat. #K151B9K-2
V-PLEX Human IL-6 Assay	Meso Scale Discovery	Cat. #K151QXD-2
V-PLEX Vascular Injury Panel 2	Meso Scale Discovery	Cat. #K15198D-2
Human TREM2 Assay	Abcam	Cat. #ab224881
Human C1q Assay	Abcam	Cat. #ab170246
Deposited data		
scRNAseq (cell data) Raw data files and metadata	This paper	GEO: GSE289565.
Mass spectrometry proteomics data (CLU WT vs KO monoculture cell data) Raw data files and metadata	This paper	Synapse: syn50208824 (https://www.synapse.org/#!Synapse:syn50208824)
Mass spectrometry proteomics data (Neurons co-cultured with CLU WT vs KO astrocytes cell data) Raw data files and metadata	This paper	Synapse: syn52502746 (https://www.synapse.org/#!Synapse:syn52502746)
Mass spectrometry proteomics data (Microglia co-cultured with CLU WT vs KO astrocytes cell data) Raw data files and metadata	This paper	Synapse: syn53190960 (https://www.synapse.org/#!Synapse:syn53190960)
RNAseq data (mouse data) Raw data files and metadata	This paper	GEO: GSE294133
Mass spectrometry proteomics data (human) Raw datafiles and clinical metadata	Vialle et al.[50] and Seifar et al.[104]	Synapse: syn5342067 (https://www.synapse.org/#!Synapse:syn5342067)
Mass spectrometry proteomics data (human) Search results and database, sample-to-sample TMT channel information, normalized data	Vialle et al.[50] and Seifar et al.[104]	Synapse: syn55225561 (https://www.synapse.org/#!Synapse:syn55225561)
snRNA-seq data (human) Raw and processed snRNA-seq data	Green et al.[51]	Synapse: syn31512863 (https://www.synapse.org/#!Synapse:syn31512863)
Experimental models: Cell lines		
HUMAN IPSC LINE: BR24	Lagomarsino et al.[80]	BR24, AJ0040
HUMAN IPSC LINE: BR33	Lagomarsino et al.[80]	BR33, AJ0047
HUMAN IPSC LINE: BR09	Lagomarsino et al.[80]	BR09, AJ0038
HUMAN IPSC LINE: BR106	This paper	BR106, AJ0098
HUMAN IPSC LINE: BR15	Lagomarsino et al.[80]	BR15, AJ0008
HUMAN IPSC LINE: BR266	This paper	BR266, AJ0210
HUMAN IPSC LINE: BR265	This paper	BR265, AJ0215
HUMAN IPSC LINE: BR68	Lagomarsino et al.[80]	BR68, AJ0095
HUMAN IPSC LINE: BR97	Lagomarsino et al.[80]	BR97, AJ0123
HUMAN IPSC LINE: BR209	This paper	BR209, AJ0162
HUMAN IPSC LINE: BR13	Lagomarsino et al.[80]	BR13, AJ0039
HUMAN IPSC LINE: BR205	This paper	BR205, AJ0152
HUMAN IPSC LINE: BR08	Lagomarsino et al.[80]	BR08, AJ0044
HUMAN IPSC LINE: BR30	Lagomarsino et al.[80]	BR30, AJ0042
HUMAN IPSC LINE: BR215	This paper	BR215, AJ0184
7889-SA (WT)	Paquet et al.[105]	N/A
7889-SA (APP^{SWE}; $PSEN1^{M146V}$)	Paquet et al.[105]	N/A
Human iPS Cell Line (Episomal, CD34+, APOE4)	Alstem cell advancement	iPSC16
Oligonucleotides		
CLU gRNA: 'GCGTGCGTAGAACTTCATGC'	This paper	N/A
Software and algorithms		
V4.4.0 of R	R Core Team[106]	https://www.rstudio.com

(*Continued on next page*)

Continued

REAGENT or RESOURCE	SOURCE	IDENTIFIER
CellRanger, v7.1.0	Zheng et al.[107]	https://www.10xgenomics.com/support/software/cell-ranger/latest
Seurat, v5.0.3	Satija et al.[108]	https://satijalab.org/seurat/
Fiji (ImageJ), v2.14.0/1.54f	Schindelin et al.[109]	https://imagej.net/software/fiji/
Prism, v10	Graphpad Software	https://www.graphpad.com
NeuronStudio, v0.9.92	Rodriguez et al.[110]	https://www.bionity.com/en/encyclopedia/Neuronstudio.html
Image Studio Lite, v4.0	Image Studio Software	https://www.licor.com/bio/image-studio/
Biorender	N/A	https://www.biorender.com
Cell Profiler, v4.1.1	Paquet et al.[105]	https://cellprofiler.org/
Other		
Shinyapp visualization of CLU WT vs KO cell data	This paper	https://youngpearselab.shinyapps.io/clu_ia/.

EXPERIMENTAL MODEL AND STUDY PARTICIPANT DETAILS

Human subject approvals

All work was performed following IRB review and approval through Partners/BWH IRB (2016P000867 and 2015P001676). Human brain material was obtained from Rush University Medical Center. ROS and MAP studies were approved by an Institutional Review Board of Rush University Medical Center. All participants signed an informed consent, an Anatomical Gift Act, and a repository consent allowing their data and biospecimens to be repurposed, and for data acquired from these samples to be published. All individuals in the ROSMAP cohorts are administered annual cognitive tests and neuropathological AD indices were acquired postmortem. For postmortem neuropathological assessments of ROS and MAP participants, measures of neuritic and diffuse plaques and neurofibrillary tangles were determined by silver stain.[49] Additionally, measures of Aβ load and paired helical filament tau tangles were measured by staining with M00872 and an antibody specific for phosphorylated tau, respectively.[52–54] The resulting neuropathological scores are composite data derived from at least five regions: inferior parietal neocortex, temporal cortex, mid-frontal cortex, hippocampus, and the entorhinal cortex. Clinical diagnosis of Alzheimer's dementia, mild cognitive impairment (MCI), and no cognitive impairment (NCI) were done as reported.[111] Cognition was measured with a comprehensive neuropsychological test battery.[112] Details regarding participant information for the TMT-MS and snRNA-seq datasets are as previously described.[50,51,104]

Sequential human brain extract preparation

Frozen angular gyrus tissue was thawed and meninges were peeled off and discarded. Aqueous TBS extracts were prepared according to the "soaking" method as previously described[113,114] with some modifications. The tissue was chopped on a McIlwain tissue chopper set to 0.05 mm width, then soaked for 30 minutes in a 5-ml Eppendorf Protein LoBind tube with nutation at 4°C in five volumes TBS (20 mM Tris, 150 mM NaCl, pH 7.4) supplemented with 5 μg/ml leupeptin, 5 μg/ml aprotinin, 2 μg/ml pepstatin, 120 μg/ml 4-benzenesulfonyl fluoride hydrochloride, and 5 mM NaF. The suspension was then centrifuged at 2,000g in a swinging-bucket rotor for 10 minutes at 4°C. The supernatants were then centrifuged in 1.5-ml LoBind tubes at 20,000g for 110 minutes at 4°C in a tabletop centrifuge. The supernatants were pooled and re-aliquoted and frozen at -80°C as the TBS soluble fraction for further analysis. The pellets were frozen at -80°C for subsequent extraction.

To create the SDS and urea extracts, a pellet from the TBS extract was thawed on ice and reweighed. The pellet was resuspended in five volumes TBS with 2% SDS. The samples were sonicated at 35% power three times for 10 seconds. They were then centrifuged again at 20,000g for 110 minutes at 4°C in a tabletop centrifuge as above. The supernatants were re- aliquoted and frozen at -80°C as the SDS extract. The pellets were resuspended in another 5 volumes of 8M urea followed by sonication, centrifugation, and aliquoting for the SDS extracts. See Table S1 for participant details (30 ROSMAP participants with European ancestry). For WB analyses depicted in Figure 1: To account for variability across blots, two samples were included on each blot and used as internal normalization controls. The CLU/β-actin values from these duplicates were used to standardize signal intensity across multiple blots.

Linkage disequilibrium and eQTL analysis

To identify genes with expression changes associated with the dosage of *CLU* SNPs, we leveraged our recently published cell subtype-specific genome-wide cis eQTL analysis of the dorsolateral prefrontal cortex from 424 ROSMAP donors.[51] Briefly, after de-novo clustering and identifying discrete astrocyte subtypes, we used Matrix eQTL v.2.3 to identify dosage-expression associations within 1 Mb of the transcription start site of each gene in all the astrocyte subtypes. We used age at death, sex, and post-mortem interval as covariates and expression and genotype principal components to account for coexpression and geographic ancestry, respectively. CLU SNPs with a minor allele frequency greater than 5%, a call rate greater than 95% and Hardy–Weinberg $P > 10-6$ were retained.

Significance was computed from a t-test and a two-step Bonferroni-FDR multiple hypothesis correction. The beta of the association is displayed in Figure 1J. Additionally, linkage disequilibrium with R2 > 0.2 in European populations for eight CLU variants (i.e., rs11787077, rs7982, rs11136000, rs2279590, rs9331888, rs9331896, rs1532278, rs9331908) was derived from TopLD database (accessed on 06/11/2024).

Longitudinal Plasma Cohort and NULISA Sequencing

Plasma samples from 46 individuals (european ancestry) enrolled in the Rush Religious Orders Study and Memory and Aging Project (ROSMAP) were obtained at three longitudinal time points (see Figure 7A; Table S7 for participant details). Protein profiling was performed by Emtherapro using the Alamar Biosciences NULISA CNS Disease Panel as previously described.[79]

Linear Regression Analysis for Longitudinal Plasma Cohort

To normalize the measurements for Alamar sequencing and MSD CLU ELISA, we first performed z-score transformation, followed by batch correction, and then calculated slopes. For each individual, we determined the slope of protein levels over time by regressing the measured levels against age at each visit. In this analysis, we used two distinct age metrics: the actual age at visit (i.e., the calendar age when the sample was collected) for the regression models, and the relative age at visit (i.e., the time elapsed since the baseline visit) for calculating the slopes. Protein levels were quantified through NULISA sequencing, and CLU levels were measured via MSD ELISA (1/4000 dilution). Individuals missing measurements at any time point were excluded from the slope analysis—this affected CLU slopes for one rs11787077 TT sample and two rs11787077 CC samples. Finally, simple linear regression was performed to assess the association between these slope values and the dosage of the CLU risk SNP rs11787077 (T/T = 0, T/C = 1, C/C = 2).

Mice

All experiments involving mice were approved by the UC Irvine Institutional Animal Care and Use Committee and conducted in accordance with ethical regulations for animal testing and research. All animals were bred by the Transgenic Mouse Facility at UCI.

To generate mice modeling the human rs2279590 variant (C57BL/6J-Clu$^{em1(CLU*)Aduci}$/J, Jackson Laboratory stock #037496), Alt-R CRISPR RNAs (TMF1353, 1354, 1355, and 1356, Table S6), tracrRNA, and CAS9 protein (HiFi Cas9 nuclease V3, Integrated DNA Technologies [IDT], Coralville, IA) were assembled into a ribonucleoprotein (RNP) complex and microinjected into C57BL/6J zygotes (Jackson Lab Stock #000664). A single-stranded DNA (ssDNA: TMF1304, Table S6) was co-injected to introduce the rs2279590 SNP mutation and replace mouse *Clu* exons 8 and 9 with their human counterparts.

G0 founder animals with the desired DNA sequence modifications were backcrossed with C57BL/6J mice, and N1 heterozygous mice were sequenced to confirm the presence of the mutant allele. These N1 heterozygous mice were further backcrossed to produce N2F1 heterozygotes, which were subsequently used to generate animals for analysis. These heterozygotes (female mice) were then crossed with 5xFAD hemizygous congenic B6J (B6.CgTg(APPSwFlLon,PSEN1*M146L*L286V)6799Vas/Mmjax, Jackson Lab Stock # 34848, MMRRC) male mice to produce N3F1 animals that were heterozygous or wildtype for CLU-2kb-KI and hemizygous or nontransgenic for 5xFAD. These N3F1 animals were used to produce N3Fx experimental and control animals by natural mating or in vitro fertilization procedures. The ensuing experimental genotypes will be further referred to as 5xFAD and 5xFAD/CLU-2kb-KI.

Genotyping

Oligonucleotides for polymerase chain reaction (PCR)-based genotyping were purchased from IDT. *CLU-2kb-KI* genotyping was performed using separate reverse primers to amplify each the mouse *Clu* wild-type allele and the *CLU-2kb-KI* allele (Forward: 5′-TTTCAAGTTTCTGGAGTGCCTACT-3′; Reverse 1: 5′-CTACGGGATGGCTGCAGAG-3′; Reverse 2: 5′-CAGTGACACCGGAAGG AACG-3′). Two fluorophore-labeled hydrolysis probes were used to detect the allelic ratio in the amplicon: one specific to the mouse *Clu* wild-type amplicon (5′-AACCCGCAGATCCATATCTG-3′-HEX) and the other to the *CLU-2kb-KI* allele (5′-GCATGGGGTCA GCTCTCTAG-3′-FAM). The relative fluorescence from each probe was quantified at the end point of the PCR cycles to determine the genotype using the allelic discrimination function of Bio-Rad CFX Maestro software (Bio-Rad, Hercules, CA).

Tissue Collection

Mice of all control and experimental genotypes (5xFAD and 5xFAD/CLU-2kb-KI) and both sexes (n=5 per sex) were used for bulk RNA sequencing and Western Blot experiments. Mice were anesthetized at 4 months of age using CO_2 inhalation. Following transcardial perfusion with 1X phosphate-buffered saline (PBS), brains were extracted, and hemispheres were separated along the midline. The left hippocampus and cortex were dissected and flash-frozen on dry ice. Samples were pulverized using a Bessman Tissue Pulverizer. Half of pulverized hippocampus and a third of pulverized cortex was used for bulk RNA sequencing and Western Blot analysis, respectively.

Induced pluripotent stem cell lines

IPSC lines were utilized following IRB review and approval through MGB/BWH IRB (#2015P001676). iPSCs were generated from cryopreserved peripheral blood mononuclear cell (PBMC) samples from autopsied participants from the ROS and MAP cohorts. iPSCs were generated using Sendai reprogramming method.[80] iPSCs undergo a rigorous quality procedure that includes a sterility check, mycoplasma testing, karyotyping, and pluripotency assays performed by the New York Stem Cell Foundation (NYSCF). iPSCs were maintained using StemFlex Medium (Thermo Fisher Scientific). All cell lines were routinely tested for mycoplasma using PCR kit (MP0035-1KT) and STR profiling to prevent potential contamination or alteration to the cell lines. iPSC cell lines harboring two

homozygous familial Alzheimer's disease mutations (APP^{SWE}/$PSEN1^{M146V}$;APP^{SWE}/$PSEN1^{M146V}$) and its isogenic WT control (Coriell Institute, catalog ID: AG07889) were obtained from NYSCF and are previously described.[115] APOE ε4/ε4 (cat#iPS16) iPSCs were obtained from Alstem.

CRISPR/Cas9 editing to generate CLU WT, HET, and KO iPSCs

The following lines were chosen for CRISPR/Cas9 mutagenesis of CLU: BR33 and BR24, two iPSC lines derived from non-cognitively-impaired individuals (male and female, respectively) from the ROSMAP cohorts. gRNA 'GCGTGCGTAGAACTTCATGC' was used to target exon 4 within the CLU sequence. The Zhang Lab CRISPR Design website (crispr.mit.edu) was used to generate guide RNAs (gRNAs) with minimal off-target effects. gRNAs were cloned into the pXPR-003 vector. hiPSCs were electroporated with the sgRNA-encoding plasmid and Cas9, cells were isolated for monoclonal selection and Sanger sequenced to determine *CLU* mutations. For each targeted iPSC line, one unedited/wildtype clone and two mutant clones (HET and KO) were chosen for downstream analyses (summarized in Figures S3A and S3B). Stem Cell Technologies hPSC Genetic Analysis kit (#07550) was used for the isogenic pairs (iPSCs) to check for karyotype abnormalities. IDT CRISPR Cas9 guide RNA design checker was used to check for any potential off-target effects.

Differentiation of iPSCs to induced astrocytes (iAs)

iPSC-derived astrocytes (iAs) were differentiated following a previously published paper[55] with minor modifications.[56,80,116] iPSCs were plated at 95k cells/cm^2 on growth factor reduced Matrigel (Corning #354230) coated plates prior to virus transduction. Then, iPSCs were transduced with three lentiviruses – Tet-O-SOX9-puro (Addgene plasmid #117269), Tet-O-NFIB-hygro (Addgene plasmid #117271), and FUdeltaGW-rtTA (Addgene plasmid #19780). The cells were then replated at 200k cells/cm2 using StemFlex Medium (Thermo Fisher Scientific) and ROCK inhibitor (10 μM) (D0). The media was changed daily with Expansion Media (EM) from days 1 to 3, and gradually switched from EM to FGF media from day 4 to day 7. On day 8, cells were dissociated using Accutase, and plated at 84k cells/cm^2 using FGF media. Doxycycline (2.5μg/ml, Sigma) was added from day 1 to the end of the differentiation, puromycin (1.25mg/ml, Gibco) was added on days 3 and 4 of the differentiation, and hygromycin (100mg/ml, InvivoGen # ant-hg-1) was added from days 4–6 of the differentiation. From day 8 to the end of differentiation day 21, cells were cultured with maturation media and fed every 2–3 days.

Induced astrocyte protocol media

- Expansion Media: DMEM/F12 (Thermo Fisher Scientific), 10% FBS, 1% N2 Supplement (Stemcell Technologies), 1% GlutaMAX (Life Technologies).
- FGF Media: Neurobasal media, 2% B27, 1% NEAA, 1% GlutaMAX, 1% FBS, 8ng/ml FGF, 5ng/ml CNTF, 10ng/ml BMP4.
- Maturation Media: 1:1 DMEM/F12 and neurobasal media, 1%N2, 1%GlutaMAX, 1% Sodium Pyruvate, 5μg/ml N-1% N2, 1% GlutaMAX, 1%Sodium Pyruvate, 5μg/ml N-N-acetyl cysteine, 5ng/ml heparin-binding EGF-like GF, 10ng/ml CNTF, 10ng/ml BMP4, 500μg/ml dbcAMP.

Differentiation of iPSCs to microglia-like cells (iMGs)

iPSC-derived microglia-like cells (iMGs) were differentiated following a previously published protocol,[117,118] with minor modifications.[80,119] iPSCs were plated on growth factor reduced Matrigel (Corning #354230) using StemFlex Medium (Thermo Fisher Scientific) and ROCK inhibitor (10 μM). From day 0 to day 12 of differentiation, StemDiff Hematopoietic Kit (StemCell Technologies) was used to generate hematopoietic precursor cells (HPCs). On day 12, cells were replated at 10k cells/cm^2 in iMG media supplemented with 3 cytokines (IL-34 (100 ng/mL, PeproTech), TGF-b1 (50 ng/mL, Militenyi Biotech), and M-CSF (25ng/mL, Thermo Fisher Scientific)). From days 12–20, iMG media with freshly added cytokines were added to the culture every other day. On day 20, cells were plated at 53k cells/cm^2 with 1:1 mixture of old media and fresh iMG media with 3 cytokines. From day 20 to day 37, iMG media with freshly added 3 cytokines were added to the culture every other day. On day 37, cells are resuspended in iMG media with five cytokines (100ng/mL IL-34, 50ng/mL TGF-β1, 25ng/mL M-CSF, 100 ng/mL, CD200 (Novoprotein) and 100ng/mL CX3CL1 (PeproTech)), supplemented every other day until day 40.

iPSC-derived microglia protocol media

- iMG media: DMEM/F12, 2X insulin-transferrin-selenite, 2X B27, 0.5X N2, 1X GlutaMAX, 1X non-essential amino acids, 400mM monothioglycerol, 5 mg/mL insulin, and 1% Pen-Strep.
- 3 cytokines: 100 ng/mL IL-34 (PeproTech), 50ng/mL TGF-b1 (Miltenyi Biotech), and 25 ng/mL M-CSF (ThermoFisher Scientific).
- 5 cytokines: 100ng/mL IL-34, 50 ng/mL TGF-b1, 25ng/mL M-CSF, 100ng/mL, CD200 (Novoprotein) and 100ng/mL CX3CL1 (PeproTech).

Differentiation of iPSCs to induced neurons (iNs)

iPSC-derived neurons (iNs) were differentiated following a previously published paper[103] with minor modifications.[80,120] iPSCs were plated at a density of 95k cells/cm^2 on plates coated with growth factor reduced Matrigel one day prior to virus transduction (Corning #354230). Then, iPSCs were transduced with three lentiviruses – pTet-O-NGN2-puro (Addgene plasmid #52047, a gift from Marius

Wernig), Tet-O-FUW-EGFP (Addgene plasmid #30130, a gift from Marius Wernig), and FUdeltaGW-rtTA (Addgene plasmid #19780, a gift from Konrad Hochedlinger). The cells were then replated at 200k cells/cm^2 using StemFlex Medium (Thermo Fisher Scientific) and ROCK inhibitor (10 μM) (day 0). The media was changed to KSR media (day 1), 1:1 of KSR and N2B media (day 2) and N2B media (day 3). On day 4, cells were dissociated using accutase, and plated at 50k cells/cm^2 using iN D4 media (NBM media +1:50 B27 + BDNF, GDNF, CNTF (10 ng/mL, PeproTech). Doxycycline (2μg/ml, Sigma) was added from day 1 to the end of the differentiation, and puromycin (5mg/ml, Gibco) was added from day 2 to the end of the differentiation. On day 3, B27 supplement (1:100) (Life Technologies) was added. From day 4 to the end of differentiation day 21, cells were cultured in iN day 4 media and fed every 2–3 days.

Induced neuron protocol media

- KSR media: Knockout DMEM, 15% KOSR, 1x MEM-NEAA, 55 mM beta-mercaptoethanol, 1x GlutaMAX (Life Technologies).
- N2B media: DMEM/F12, 1x GlutaMAX (Life Technologies), 1x N2 supplement SB (Stemcell Technologies), 0.3% dextrose (D-(+)-glucose, Sigma).
- NBM media: Neurobasal medium, 0.5x MEM-NEAA, 1x GlutaMAX (Life Technologies), 0.3% dextrose (D-(+)-glucose, Sigma).

iPSC Microglia-Astrocyte and Neuron-Astrocyte co-cultures

iNs and iAs were differentiated to day 20 as described above. iMGs were seeded at 53k cells/cm^2. On day 20, iAs were dissociated and replated to transwell inserts (non-contact) or on top of iN cultures (contact) at 47k cells/cm^2. For non-contact cultures, on day 21, iAs were co-cultured with iMGs or iNs by transferring transwell inserts into the wells containing iMG cultures. On this day, the medium was switched to BrainPhys media + 5 cytokines.

iPSC Microglia-Astrocyte and Neuron-Astrocyte co-culture media

- BrainPhys Neuronal Medium (StemCell Technology, 5792) + NeuroCult SM1 Neuroonal Supplement (StemCell Technology, 5711) + 100ng/mL IL-34, 50ng/mL TGF-β1, 25ng/mL M-CSF, 100ng/mL, CD200 (Novoprotein) and 100ng/mL CX3CL1 (Peprotech).

iSPC-Astrocyte-Neuron-Microglia tri-culture

iNs and iAs were differentiated to day 20 and iMGs were differentiated to day 40 as described above. Initially, iNs, iMGs, and iAs are seeded at 53k cells/cm^2. On day 20, iAs are dissociated using accutase and are replated on top of iN cultures at a density of 47k cells/cm^2 in iA maturation media + 1:50 B27 + BDNF, GDNF (10 ng/mL, Peprotech) + Doxycycline (2.5μg/ml, Sigma) + ROCK inhibitor (10 μM). On day 21 (day 40 of iMG differentiation), iMGs are dissociated and replated on top of iN-iA co-cultures at a density of 42k cells/cm^2 in BrainPhys media + 5 cytokines. All three cell types were then co-cultured together for an additional six days. The final ratio of cells at the end of co-culture is approximately 5 neurons: 1 astrocyte: 3 microglia. See Figures S5M–S5N.

iPSC-tri-culture media

- BrainPhys Neuronal Medium (StemCell Technology, 5792) + NeuroCult SM1 Neuroonal Supplement (StemCell Technology, 5711) + 100ng/mL IL-34, 50ng/mL TGF-β1, 25ng/mL M-CSF, 100ng/mL CD200 (Novoprotein) and 100ng/mL CX3CL1 (Peprotech).

METHOD DETAILS

Western blotting

Cells were lysed with RIPA lysis buffer (Thermo Fisher Scientific #89900) with the protease inhibitor (Complete TM mini protease inhibitor, Roche) and phosphatase inhibitor (phosphoSTOP, Roche) added freshly before the lysis. Cells were lysed for 30 minutes on ice before transferring lysates to microcentrifuge tubes. Cell debris was pelleted by centrifugation (13,000 x g) for 10 minutes at 4°C. Supernatant (cell lysate) was collected and stored at -20°C until use. Protein concentration in cell lysate samples was determined with the Pierce BCA Protein Assay kit (ThermoFisher, #23225). Cell lysates were prepared with 4X LI-COR loading buffer (Fisher Scientific, #NC9779096) and 2.5% β-mercaptoethanol, centrifuged, and incubated at 95°C for 10 minutes. Samples were resolved using Novex NuPAGE™ 4-12% Bis-Tris gels (ThermoFisher, #NP0336BOX) and NuPAGE™ 1X MOPS-SDS or MES-SDS running buffer (ThermoFisher, #NP0001). Gel electrophoresis was run at 200V for 50 minutes. SeeBlue Plus2 (ThermoFisher, #LC5925) pre-stained protein standard was used for evaluation of molecular weight. The gel was extracted and transferred to a nitrocellulose membrane by incubation with 20% methanol tris-glycine transfer buffer at 400mA for two hours. The transferred blot was blocked with Odyssey blocking buffer (LI-COR, #927-50100) for 1 hour at room temperature with agitation and incubated with primary antibody (diluted in blocking buffer) overnight at 4°C with agitation. Blots were incubated with LI-COR secondary antibody diluted 1:10,000 in TBST for 1 hour at room temperature with agitation. Blots were washed twice (10 minutes per wash) with TBST and stored in 1X TBS until imaging. Blots were imaged on a LI-COR Odyssey machine and quantified using ImageStudio software.

Immunocytochemistry

Cells were washed with PBS and then fixed with 4% paraformaldehyde (PFA, Sigma) for 15 minutes at room temperature. Cells were blocked in 2% donkey serum (Jackson Immunoresearch Laboratories) and 0.2% Triton-X-100 (Sigma) in PBS for 1 hour at room

temperature with agitation. For cultures with microglia, 0.04% PFA was spiked into the wells prior to removing the conditioned media. The plates were then placed at 37°C for 20 minutes, allowing for a gentle initial fixation to avoid microglia loss during the fixation process. Primary antibodies were diluted in a fresh donkey serum blocking buffer and cells were incubated with primary antibody solution overnight at 4°C. Then, cells were washed with PBS three times, incubated with secondary antibodies for 1 hour at room temperature with agitation, and then washed with PBS three times. Cells were treated with DAPI stain (1:1000 dilution) for 10 minutes at room temperature with agitation, followed by a final wash to prepare for imaging. Images were taken on a Zeiss LSM710 Confocal, Andor Dragonfly 600 Spinning Disk Confocal, or Zeiss LSM880 + Fast Airyscan Confocal microscope. For the representative images shown in Figure 8A, the 'Remove Outliers' function was used in ImageJ with a radius of 5 pixels and a threshold of 50, applied uniformly across all images. This step was used only to remove bright pixel artifacts that were introduced during antibody staining. All images were processed in ImageJ with brightness and contrast adjustments applied consistently across all images for visualization of representative cultures throughout conditions.

Antibodies for western blot and immunocytochemistry

Antigen	Host	ICC/WB	Dilution	Vendor	Catalog #
AT8 (MAPT) P202, P205	Mouse	WB	1:250	ThermoFisher	MN1020
CLU	Rabbit	WB	1:1000	Abcam	ab92548
GAPDH	Mouse	WB	1:10000	ProteinTech	60004
GFAP	Chicken	ICC and WB	1:1000	Abcam	ab4672
IBA1	Goat	ICC and WB	1:500	Abcam	AB5076
ICAM1	Rabbit	WB	1:1000	CST	4915
IκBα	Mouse	WB	1:1000	CST	4814S
S100B	Rabbit	ICC	1:1000	Abcam	ab52642
TAU (MAPT)	Rabbit	WB	1:1000	CST	46687S
TREM2	Rabbit	WB	1:1000	Abcam	ab209814
TUJ1	Chicken	ICC and WB	1:1000	Millipore	MAB1637
Vimentin	Mouse	ICC	1:1000	Millipore	CBL202
CD44	Mouse	WB and ICC	1:1000	Abcam	ab253530
VGLUT2	Mouse	ICC	1:1000	Abcam	ab79157
HOMER1	Rabbit	ICC	1:1000	Synaptic Systems	160003
NeuN	Rabbit	ICC	1:500	Abcam	ab177487
TUJ1	Chicken	ICC	1:500	Novus	nb100-1612
pTAU 217	Rabbit	WB	1:1000	GeneTex	GTX135775
pTAU 214	Rabbit	WB	1:1000	Cell Signaling	77348

qPCR

At iA day 21, cells were harvested and RNA was purified using Purelink RNA Mini kit (Invitrogen). cDNA was generated using SuperScript II (Invitrogen). qPCR was performed using Power SYBR™ Green Master Mix and run on ViiA7 system (Applied Biosystems). Samples were assayed with 3 technical replicates and analyzed using the ΔΔCt method and expression was normalized to GAPDH expression.

Primers

Target	Species	For/Rev	Sequence
GAPDH	Human	F	GGGAGCCAAAAGGGTCATC
GAPDH	Human	R	TGGTTCACACCCATGACGAA
CLU	Human	F	TGCGGATGAAGGACCAGTGTGA
CLU	Human	R	TTTCCTGGTCAACCTCTCAGCG
C3	Human	F	GTGGAAATCCGAGCCGTTCTCT
C3	Human	R	GATGGTTACGGTCTGCTGGTGA
CCL2	Human	F	AGAATCACCAGCAGCAAGTGTCC

(*Continued on next page*)

Continued

Target	Species	For/Rev	Sequence
CCL2	Human	R	TCCTGAACCCACTTCTGCTTGG
IL6	Human	F	AGACAGCCACTCACCTCTTCAG
IL6	HUman	R	TTCTGCCAGTGCCTCTTTGCTG

ELISAs

48hr conditioned media was collected prior to harvest. Extracellular proteins were measured following manufacturer instructions. Samples were normalized to total protein concentration as determined by the Pierce BCA Protein Assay kit (ThermoFisher, #23225). For C1q ELISA in tri-culture, samples were normalized to IBA1.

ELISA kits used for extracellular measurements

Analyte(s)	Species	Vendor	MSD Assay Kit	Catalog #
C3	Human	MesoScale Discoveries	R-PLEX	F21XY-3
CLU	Human	MesoScale Discoveries	U-PLEX	K151B9K-2
IL-6	Human	MesoScale Discoveries	V-PLEX	K151QXD-2
ICAM-1, VCAM-1, CRP, SAA	Human	MesoScale Discoveries	V-PLEX Vascular Injury Panel 2	K15198D-2
APOE	Human	MesoScale Discoveries	R-PLEX	K1512IR-2
C1q	Human	Abcam	N/A	ab170246
TREM2	Human	Abcam	N/A	ab224881

Cell culture treatments relating to NfκB inhibition or activation

For iA monocultures, 24hrs prior to harvest, cells were fed with iA media containing the following: 500nM IKK Inhibitor VII (Millipore, 401486) as previously described[121] or 5ng/ml TNF (Fisher Scientific, 210TA020) + 1ng/ml IL1β (Fisher Scientific, 201LB005) as previously described.[56] The vehicles were DMSO for IKK Inhibitor or 0.1% BSA in PBS for TNF and IL1β. For iA-iMG-iN, iA-iN, and iMG cultures, 72hrs prior to harvest, cells were fed with tri-culture medium containing the following: 400ng/mL C1q (MyBioSource, MBS147305) as previously described.[36]

Canonical NfκB luciferase reporter assay

For the NfκB luciferase assay, two reporter plasmids were used: (1) pRL-CMV, encoding *Renilla* luciferase controlled by a CMV promoter, and (2) pGL4.32[*luc2P*/NF-κB-RE/Hygro], encoding Firefly luciferase under a minimal promoter with an NfκB response element (Promega, #E2261 and #E849A, respectively). Day 18 iAs were transfected with the two reporter plasmids using the Amaxa P3 Primary Cell 4D-Nucleofector Kit (Lonza, #V4XP-3024) at a ratio of 2μg pGL4.49[*luc2P*/NF-κB-RE/Hygro] and 0.2μg pRL-CMV per 1 million cells. Nucleofected cells were plated in white-walled 96-well plates (Corning #3917) at 100k cells/well. 48 hrs post-nucleofection, the media was replaced with vehicle (0.1% BSA) or 5ng/mL TNF + 1ng/ml IL1β (Fisher Scientific, 210TA020) as a positive control. Cells were treated for 24 hours before lysing the cells and measuring Firefly and *Renilla* luciferase signal using the Dual-Luciferase Reporter Assay System (Promega, #E1910). Luciferase signal was measured using a spectrophotometer, integrating the luminescence signal for 5 seconds. Baseline canonical NfκB signaling was calculated by dividing Firefly signal / *Renilla* signal in vehicle-treated samples.

CLU overexpression

On day 18 of iA differentiation, cells were dissociated in accutase (diluted 1:3 in PBS) and transfected (as described in the previous section) with 2 μg pmax-CMV>eGFP (Lonza, #V4XP-3032) or 2 μg human tagged *CLU* (pRP[Exp]-CMV>eGFP-CAG>hCLU [NM_001831.4]). 72 hours following transfection, conditioned media was collected and cells were harvested as described in previous sections.

Synaptosome Isolation and pHrodo Conjugation

Synaptosomes were isolated from mouse brains using Syn-PER Reagent (Thermo Fisher Scientific), following the manufacturer's protocol and as previously described[77] with minor modifications. Briefly, phosphatase and protease inhibitors were added to Syn-PER at a concentration of 1 tablet per 10 mL. Mouse brain tissue was weighed, and 10 mL of Syn-PER Reagent was added per gram of tissue. The tissue was homogenized on ice using a Dounce homogenizer with ~10 slow strokes. The homogenate was centrifuged at 1200 × g for 10 minutes at 4°C to remove debris, and the supernatant was collected. This was further centrifuged at 15,000 × g for 20 minutes at 4°C to pellet the synaptosomes. The final pellet was resuspended in 0.1 M sodium bicarbonate buffer

(pH 8.3–8.4) at a concentration of 50 mg/mL. For pHrodo conjugation, the synaptosome suspension was incubated with 3 μM of amine-reactive pHrodo Green STP dye (Thermo Fisher Scientific) for 45 minutes at room temperature in the dark. The mixture was diluted 1:10 in DPBS and centrifuged at 2500 × g for 5 minutes at 4°C. The pellet was washed twice with DPBS and resuspended in sterile-filtered brainphys media to a final concentration of 50 mg/mL. Synaptosomes were used for treatments at a final concentration of 1 mg/mL.

Flow Cytometry

Phagocytosis assays were conducted using iPSC-derived microglia-astrocyte co-cultures treated with pHrodo-labeled synaptosomes. Prior to flow cytometry, live imaging was performed using the Incucyte platform to assess pHrodo signal integrity. pHrodo intensity was measured and normalized to the total cell area to quantify synaptosome uptake. For flow cytometry, iMGs were gently dissociated with PBS and centrifuged at 500 × g for 5 minutes at 4°C. Cells were stained with Zombie Violet (BioLegend) for live/dead discrimination and incubated on ice for 20 minutes, protected from light. After washing, cells were stained with PE-conjugated anti-P2RY12 (BioLegend, #392104, 1:20) and PE-Cy7-conjugated anti-CD11b (BioLegend, #101215, 1:200) antibodies in FACS buffer (HBSS supplemented with 10% FBS, 25 mM HEPES, and 2 mM EDTA). Staining was performed for 30–60 minutes on ice, followed by fixation with 4% paraformaldehyde for 20 minutes. Samples were analyzed on a Fortessa flow cytometer equipped with 355 nm, 488 nm, 561 nm, and 640 nm lasers. Phagocytosis was quantified as the percentage of pHrodo-positive cells within live, P2RY12+, and CD11b+ gated populations. Data acquisition and analysis were performed using FlowJo software, with compensation applied for multicolor fluorescence detection.

TMT proteomic and data analysis

Sample processing

iAs were plated in 6-wells (1 million cells/well) and differentiated to day 21. Media was removed from the wells and iAs were washed 2x with ice-cold DPBS. Samples were processed as previously described.[122,123] Cells were lysed in 250 μL of urea lysis buffer (8 M urea, 100 mM NaHPO4, pH 8.5) with the protease inhibitor (Complete TM mini protease inhibitor, Roche) and phosphatase inhibitor (phosphoSTOP, Roche) added freshly before the lysis. All homogenization was performed using a Bullet Blender (Next Advance) according to manufacturer protocols. Briefly, each tissue piece was added to urea lysis buffer in a 1.5 mL Rino tube (Next Advance) harboring 750 mg stainless steel beads (0.9–2 mm in diameter) and blended twice for 5 min intervals in the cold room (4 °C). Protein supernatants were transferred to 1.5 mL Eppendorf tubes and sonicated (Sonic Dismembrator, Fisher Scientific) 3 times for 5 s with 15 s intervals of rest at 30% amplitude to disrupt nucleic acids and subsequently vortexed. Protein concentration was determined by the bicinchoninic acid (BCA) method, and samples were frozen in aliquots at −80 °C. Protein homogenates (50 μg) treated with 1 mM dithiothreitol (DTT) at 25 °C for 30 min, followed by 5 mM iodoacetamide (IAA) at 25 °C for 30 min in the dark. Protein mixture was digested overnight with 1:100 (w/w) lysyl endopeptidase (Wako) at room temperature. The samples were then diluted with 50 mM NH4HCO3 to a final concentration of less than 2 M urea and then and further digested overnight with 1:50 (w/w) trypsin (Promega) at 25 °C. Resulting peptides were desalted with a Sep-Pak C18 column (Waters) and dried under vacuum.

Tandem mass tag (TMT) labeling

Peptides were reconstituted in 100μl of 100mM triethyl ammonium bicarbonate (TEAB) and labeling performed using TMTPro isobaric tags (Thermofisher Scientific, A44520) as previously described.[122,124] Briefly, the TMT labeling reagents were equilibrated to room temperature, and anhydrous ACN (200mL) was added to each reagent channel. Each channel was gently vortexed for 5min, and then 20mL from each TMT channel was transferred to the peptide solutions and allowed to incubate for 1hr at room temperature. The reaction was quenched with 5%(v/v) hydroxylamine (5 mL) (Pierce). All 16 channels were then combined and dried by SpeedVac (LabConco) to approximately 100mL and diluted with 1 mL of 0.1% (v/v) TFA, then acidified to a final concentration of 1% (v/v) FA and 0.1% (v/v) TFA. Peptides were desalted with a 60 mg HLB plate (Waters). The eluates were then dried to completeness. High pH fractionation was performed essentially as described[125] with slight modification. Dried samples were re-suspended in high pH loading buffer (0.07% v/v NH4OH, 0.045% v/v FA, 2% v/v ACN) and loaded onto a Water's BEH (2.1mm 3 150mm with 1.7 mm beads). An Thermo Vanquish UPLC system was used to carry out the fractionation. Solvent A consisted of 0.0175% (v/v) NH_4OH, 0.01125% (v/v) FA, and 2% (v/v) ACN; solvent B consisted of 0.0175% (v/v) NH_4OH, 0.01125% (v/v) FA, and 90% (v/v) ACN. The sample elution was performed over a 25 min gradient with a flow rate of 0.6 mL/min with a gradient from 0% to 50% B. A total of 96 individual equal volume fractions were collected across the gradient and dried to completeness using a vacuum centrifugation.

Data processing protocol

All raw files were searched using Thermo's Proteome Discoverer suite (version 2.4.1.15) with Sequest HT. The spectra were searched against a human UniProt database downloaded August 2020 (86395 target sequences). Search parameters included 10ppm precursor mass window, 0.05 Da product mass window, dynamic modifications methionine (+15.995 Da), deamidated asparagine and glutamine (+0.984 Da), phosphorylated serine, threonine, and tyrosine (+79.966 Da), and static modifications for carbamidomethyl cysteines (+57.021 Da) and N-terminal and Lysine-tagged TMT (+304.207 Da). Percolator was used to filter PSMs to 0.1%. Peptides were grouped using strict parsimony and only razor and unique peptides were used for protein level quantitation. Reporter ions were quantified from MS2 scans using an integration tolerance of 20 ppm with the most confident centroid setting. Only unique and razor (i.e., parsimonious) peptides were considered for quantification. Abundance data were $\log_2$ transformed and batch effects were regressed using ComBat[123] Differential expression was calculated using the DEP package in R.[126]

Gene set enrichment analysis (GSEA)

Gene set enrichment analysis (queried against the Broad Hallmark gene set) was performed using the R package fgsea[127] and results were plotted using the R package ggplot2. Custom.gmt files were imported using fgsea. For reactive astrocyte signaling targets, the differential expression results of TNF + IL1β-treated vs. vehicle-treated iAs were ranked ($-\log_{10}$ adjusted p-value * $\log_2$ fold change). The top 250 upregulated genes with stimulation were used as the "Reactive Astrocyte" target gene set.

Dissociation for single cell RNA sequencing and library generation and analysis

All media were removed from both culture conditions (WT iMG + WT iA + WT iN, WT iMG + KO iA + WT iN) and the samples were processed as previously described with minor modifications.[119] Briefly, cells were dissociated with a 1:1 mixture of warm trypsin-EDTA:cold StemPro Accutase Cell Dissociation Reagent for 10min at 37°C. Trypsin was quenched with trypsin Neutralization Solution (ScienCell, 0113-2) prior to collection of cell suspension. Four independent culture wells were combined for each culture condition. Cell suspensions were centrifuged for 5 min at 300 x *g* and resuspended in 1 mL of BrainPhys media. The cell pellet was triturated gently with a p1000 tip and passed through a 40μM Flowmi Cell Strainer (Millipore, BAH136800040-50) to remove debris. Cell suspensions were centrifuged at 200 rcf for 5min and resuspended in 0.04% BSA in PBS. Washes were repeated two more times. At the end of the final wash, cell suspension was passed through another 40μM Flowmi Cell Strainer. Each triple-culture was loaded onto an individual 10X Chromium Chip well (60,000 cells per well) and resulting emulsions were used to generate scRNA-seq libraries using the Chromium Next GEM Single Cell 3′ v3.1 chemistry.

Libraries were multiplexed and sequenced on a NovaSeq to an average depth of >20K reads per filtered barcode before filtering. Fastq files were mapped using the 10xgenomics Cellranger (v7.0.0) pipeline and a GRCh38 index and resulted in an average of >4K mapped and filtered reads per cell. Mappings and counts were analyzed using the Seurat package (v5.0.3) in R (v4.4.1) using RStudio (v1.4.1103). Briefly, imported Cellranger data were filtered to remove cells with <3000 or > 10000 mapped genes and with > 20% mapping to mitochondrial genes, and to remove suspected doublets. The remaining dataset has 52,078 cells (17,479 iMGs, 33,837 iNs, and 762 iAs) with an average number of mapped genes detected per cell of 1,924 for iMGs, 2,309 for iNs, and 2,684 for iAs, and average total unique molecular identifiers (UMIs) per cell of 3,644 iMGs, 4,199 iNs, and 5,477 iAs. After filtering, normalized and scaled data were clustered using the 3000 most highly variable features. Uniform Manifold Approximation and Projection (UMAP) was run on the first 20 principal components. DEGs between cell groups were identified using FindMarkers function in Seurat using the Wilcoxon Rank Sum test with multiple comparisons adjusted (FDR) *p*-value cutoff of 0.05.

Bulk RNA-sequencing (RNA-seq)

Frozen tissues were lysed and homogenized using the TissueLyser II (Qiagen, Germantown, MD). Total RNA was extracted with the RNeasy Mini Kit and treated with the RNase-Free DNase Set on the QIAcube (Qiagen) liquid handling platform. RNA integrity was assessed using the Qubit RNA IQ Assay (Life Technologies), and samples with an RNA integrity number (RIN) of $\geq$7.0 were selected for cDNA synthesis. cDNA synthesis, amplification, library construction, and sequencing were performed by Novogene (Sacramento, CA) using Illumina NovaSeq and HiSeq platforms with paired-end 150 bp (PE 150) sequencing strategy.

Fastq files were assessed for quality using fastqc. Reads were pseudo-aligned using Salmon[128] and imported into DESeq2[129] for differential expression analysis. Counts were normalized, filtered for low abundance transcripts, and batch effects were regressed using ComBat in the sva package.[123] Principal component analysis (PCA) was performed on the batch-corrected, variance-stabilized expression matrix using the R function prcomp.[106] Differential expression was assessed using the DESeq2 package in R. Gene set enrichment was calculated (queried against the M5 Gene Ontology pathway database) using the R package fgsea.[127] Genes were ranked according to $-\log_{10}$(p-value)*sign of the $\log_2$ fold change. Heatmaps were produced for using the R package pheatmap with color palettes from the R package Seurat.

Dendritic Spine Imaging and Analysis

Wells of a 96-well plate fixed with 4% paraformaldehyde underwent dendritic spine labeling using the fluorescent dye 1,1′-dioctadecyl-3,3,3′,3′-tetramethylindocarbocyanine perchlorate (DiI, Invitrogen Cat #D282) as previously described.[130] Briefly, PBS was removed from each well, and forceps were used to obtain and sprinkle 3-5 DiI crystals across each well. A small amount (~10μL) of PBS was added to the edge of each well to avoid drying and peeling of cells. Plates were then incubated on an orbital shaker for 10 minutes at room temperature. Following incubation, wells were washed 2-3 times with PBS, and then wells were left in PBS overnight at 4°C. Approximately 12-18 hours later, plates were removed and washed three times (5 min) with diH20 at room temperature. PBS was added to each well, the plates were covered, and incubated at 4°C for at least 72 hours prior to imaging to allow for complete dye incorporation into the cells. Images of neuronal dendrites were obtained using the Super Resolution Airyscan function on a Zeiss LSM880 + Fast Airyscan Confocal microscope. Five dendrite images per well were collected using a 63X (oil immersion) objective at 50nm pixel sizes with 0.2um z-steps, followed by standard Airyscan image processing in Zeiss ZenBlack software. Images were exported as TIFF format (in ImageJ version 2.14.0/1.54f) and imported into NeuronStudio for analysis of dendritic spine densities and morphologies. Spine density measurements were acquired by reconstructing the dendritic cable to acquire the length of each imaged dendrite, followed by manual identification of spines for each dendrite. Mean densities were obtained for each dendrite within a well of a 96-well plate, and final data were analyzed with each well representing an individual data point.

Cumulative distributions of assigned spine head diameters (HEAD.DIAMETER) and neck lengths (MAX.DTS) were analyzed by Komogorov-Smirnov tests to evaluate statistical differences of spine morphologies. The data was blinded prior to analysis.

Synapse Imaging and quantification

Coverslips fixed with 4% paraformaldehyde underwent synapse immunolabeling using antibodies against a postsynaptic marker (HOMER1) and presynaptic marker (VGLUT2) along TUJ1-marked neurites. Images were obtained using the Andor Dragonfly 600 Spinning Disk Confocal. Five images per coverslip were collected using a 40X (oil immersion) objective, and were subsequently analyzed using CellProfiler.[131] Using the software's primary object identification module, individual puncta corresponding to HOMER1 and VGLUT2 were detected. Co-localization analysis was performed by measuring the overlap between HOMER1 and VGLUT2 puncta, with an overall threshold of 80% as a proxy for synaptic sites. Additionally, puncta were required to be located on TUJ1-marked dendrites. For objects meeting both the co-localization and dendrite criteria, the number of puncta and area of each punctum was quantified and normalized to the total neurite area.

Data visualization

Schematics were generated using Biorender. Graphs and heat maps were generated using R Studio[106] or GraphPad Prism 10.

QUANTIFICATION AND STATISTICAL ANALYSIS

Information regarding statistical analyses can be found in the figure legends. All statistical tests were performed using GraphPad Prism 10 or R Studio. All data is shown as mean ± SEM. Comparisons between two groups were using student's t test, and comparisons between more than two groups were analyzed using one-way or two-way ANOVA followed by Tukey's or Sidak's post-hoc test. Pearson correlation method (linear relationship) was used for correlation analyses.